7. Solomon, B. D. *et al.* Mutations in ZIC2 in human holoprosencephaly: description of a Novel ZIC2 specific phenotype and comprehensive analysis of 157 individuals. *J Med Genet* **47**, 513–524 (2010).
8. Nagai, T. *et al.* Zic2 regulates the kinetics of neurulation. *Proc Natl Acad Sci U S A* **97**, 1618–1623 (2000).
9. Aruga, J., Inoue, T., Hoshino, J. & Mikoshiba, K. Zic2 controls cerebellar development in cooperation with Zic1. *J Neurosci* **22**, 218–225 (2002).
10. Inoue, T., Ota, M., Mikoshiba, K. & Aruga, J. Zic2 and Zic3 synergistically control neurulation and segmentation of paraxial mesoderm in mouse embryo. *Dev Biol* **306**, 669–684 (2007).
11. Inoue, T., Ogawa, M., Mikoshiba, K. & Aruga, J. Zic deficiency in the cortical marginal zone and meninges results in cortical lamination defects resembling those in type II lissencephaly. *J Neurosci* **28**, 4712–4725 (2008).
12. Ogura, H., Aruga, J. & Mikoshiba, K. Behavioral abnormalities of Zic1 and Zic2 mutant mice: implications as models for human neurological disorders. *Behav Genet* **31**, 317–324 (2001).
13. Freedman, R. Schizophrenia. *N Engl J Med* **349**, 1738–1749 (2003).
14. Ross, C. A., Margolis, R. L., Reading, S. A., Pletnikov, M. & Coyle, J. T. Neurobiology of schizophrenia. *Neuron* **52**, 139–153 (2006).
15. Jaaro-Peled, H., Ayhan, Y., Pletnikov, M. V. & Sawa, A. Review of pathological hallmarks of schizophrenia: comparison of genetic models with patients and nongenetic models. *Schizophr Bull* **36**, 301–313 (2010).
16. Steen, R. G., Mull, C., McClure, R., Hamer, R. M. & Lieberman, J. A. Brain volume in first-episode schizophrenia: systematic review and meta-analysis of magnetic resonance imaging studies. *Br J Psychiatry* **188**, 510–518 (2006).
17. Vita, A., De Peri, L., Silenzi, C. & Dieci, M. Brain morphology in first-episode schizophrenia: a meta-analysis of quantitative magnetic resonance imaging studies. *Schizophr Res* **82**, 75–88 (2006).
18. Ellison-Wright, I., Glahn, D. C., Laird, A. R., Thelen, S. M. & Bullmore, E. The anatomy of first-episode and chronic schizophrenia: an anatomical likelihood estimation meta-analysis. *Am J Psychiatry* **165**, 1015–1023 (2008).
19. Karayiorgou, M., Simon, T. J. & Gogos, J. A. 22q11.2 microdeletions: linking DNA structural variation to brain dysfunction and schizophrenia. *Nat Rev Neurosci* **11**, 402–416 (2010).
20. Desbonnet, L., Waddington, J. L. & Tuathaigh, C. M. Mice mutant for genes associated with schizophrenia: common phenotype or distinct endophenotypes? *Behav Brain Res* **204**, 258–273 (2009).
21. Jaaro-Peled, H. *et al.* Neurodevelopmental mechanisms of schizophrenia: understanding disturbed postnatal brain maturation through neuregulin-1-ErbB4 and DISC1. *Trends Neurosci* **32**, 485–495 (2009).
22. Kellendonk, C., Simpson, E. H. & Kandel, E. R. Modeling cognitive endophenotypes of schizophrenia in mice. *Trends Neurosci* **32**, 347–358 (2009).
23. Pineda-Alvarez, D. E., Dubourg, C., David, V., Roessler, E. & Muenke, M. Current recommendations for the molecular evaluation of newly diagnosed holoprosencephaly patients. *Am J Med Genet C Semin Med Genet* **154C**, 93–101 (2010).
24. Brown, L. Y. *et al.* Holoprosencephaly due to mutations in ZIC2: alanine tract expansion mutations may be caused by parental somatic recombination. *Hum Mol Genet* **10**, 791–796 (2001).
25. Orioli, I. M. *et al.* Identification of novel mutations in SHH and ZIC2 in a South American (ECLAMC) population with holoprosencephaly. *Hum Genet* **109**, 1–6 (2001).
26. Dubourg, C. *et al.* Molecular screening of SHH, ZIC2, SIX3, and TGIF genes in patients with features of holoprosencephaly spectrum: Mutation review and genotype-phenotype correlations. *Hum Mutat* **24**, 43–51 (2004).
27. Roessler, E. *et al.* The full spectrum of holoprosencephaly-associated mutations within the ZIC2 gene in humans predicts loss-of-function as the predominant disease mechanism. *Hum Mutat* **30**, E541–554 (2009).
28. Aruga, J. *et al.* A wide-range phylogenetic analysis of Zic proteins: implications for correlations between protein structure conservation and body plan complexity. *Genomics* **87**, 783–792 (2006).
29. Pavletich, N. P. & Pabo, C. O. Crystal structure of a five-finger GLI-DNA complex: new perspectives on zinc fingers. *Science* **261**, 1701–1707 (1993).
30. Ramensky, V., Bork, P. & Sunyaev, S. Human non-synonymous SNPs: server and survey. *Nucleic Acids Res* **30**, 3894–3900 (2002).
31. Mizugishi, K., Aruga, J., Nakata, K. & Mikoshiba, K. Molecular properties of Zic proteins as transcriptional regulators and their relationship to GLI proteins. *J Biol Chem* **276**, 2180–2188 (2001).
32. Mizugishi, K. *et al.* Myogenic repressor I-mfa interferes with function of Zic family proteins. *Biochem Biophys Res Comm* **320**, 233–240 (2004).
33. Ishiguro, A., Ideta, M., Mikoshiba, K., Chen, D. J. & Aruga, J. ZIC2-dependent transcriptional regulation is mediated by DNA-dependent protein kinase, poly(ADP-ribose) polymerase, and RNA helicase A. *J Biol Chem* **282**, 9983–9995 (2007).
34. Arguello, P. A. & Gogos, J. A. Modeling madness in mice: one piece at a time. *Neuron* **52**, 179–196 (2006).
35. Stefansson, H. *et al.* Neuregulin 1 and susceptibility to schizophrenia. *Am J Hum Genet* **71**, 877–892 (2002).
36. O'Tuathaigh, C. M. *et al.* Phenotypic characterization of spatial cognition and social behavior in mice with 'knockout' of the schizophrenia risk gene neuregulin 1. *Neuroscience* **147**, 18–27 (2007).
37. Pletnikov, M. V. *et al.* Inducible expression of mutant human DISC1 in mice is associated with brain and behavioral abnormalities reminiscent of schizophrenia. *Mol Psychiatry* **13**, 173–186, 115 (2008).
38. Hikida, T. *et al.* Dominant-negative DISC1 transgenic mice display schizophrenia-associated phenotypes detected by measures translatable to humans. *Proc Natl Acad Sci U S A* **104**, 14501–14506 (2007).
39. Wen, L. *et al.* Neuregulin 1 regulates pyramidal neuron activity via ErbB4 in parvalbumin-positive interneurons. *Proc Natl Acad Sci U S A* **107**, 1211–1216, doi:10.1073/pnas.0910302107 (2010).
40. Shen, S. *et al.* Schizophrenia-related neural and behavioral phenotypes in transgenic mice expressing truncated Disc1. *J Neurosci* **28**, 10893–10904 (2008).
41. Chen, X. W. *et al.* DTNBP1, a schizophrenia susceptibility gene, affects kinetics of transmitter release. *J Cell Biol* **181**, 791–801 (2008).
42. Picciotto, M. R., Alreja, M. & Jentsch, J. D. in *Neuropsychopharmacology, the fifth generation of progress* (eds K. L. Davis, D. Charney, J. T. Coyle, & C. Nemerroff) 3–14. (Lippincott Williams & Wilkins, 2002).
43. Ross, R. G. *et al.* Research review: Cholinergic mechanisms, early brain development, and risk for schizophrenia. *J Child Psychol Psychiatry* **51**, 535–549 (2010).
44. Lodge, D. J., Behrens, M. M. & Grace, A. A. A loss of parvalbumin-containing interneurons is associated with diminished oscillatory activity in an animal model of schizophrenia. *J Neurosci* **29**, 2344–2354 (2009).
45. Gonzalez-Burgos, G., Hashimoto, T. & Lewis, D. A. Alterations of cortical GABA neurons and network oscillations in schizophrenia. *Curr Psychiatry Rep* **12**, 335–344.
46. Bear, M. F., Connors, B. W. & Paradiso, M. A. in *Neuroscience, exploring the brain* 572–583. (Lippincott Williams & Wilkins, 2007).
47. Vochteloo, J. D. & Koolhaas, J. M. Medial amygdala lesions in male rats reduce aggressive behavior: interference with experience. *Physiol Behav* **41**, 99–102 (1987).
48. Toth, M., Fuzesi, T., Halasz, J., Tulogdi, A. & Haller, J. Neural inputs of the hypothalamic "aggression area" in the rat.*Behav Brain Res* **215**, 7–20 (2010).
49. Inoue, T., Ota, M., Ogawa, M., Mikoshiba, K. & Aruga, J. Zic1 and Zic3 regulate medial forebrain development through expansion of neuronal progenitors. *J Neurosci* **27**, 5461–5473 (2007).
50. Katayama, K. *et al.* Slitrk1-deficient mice display elevated anxiety-like behavior and noradrenergic abnormalities. *Mol Psychiatry* **15**, 177–184, doi:10.1038/mp.2008.97 (2010).
51. Araya, R. *et al.* Loss of M5 muscarinic acetylcholine receptors leads to cerebrovascular and neuronal abnormalities and cognitive deficits in mice. *Neurobiol Dis* **24**, 334–344 (2006).
52. Yushkevich, P. A. *et al.* User-guided 3D active contour segmentation of anatomical structures: significantly improved efficiency and reliability. *Neuroimage* **31**, 1116–1128 (2006).
53. Paxinos, G. & Franklin, K. B. J. *The mouse brain in stereotaxic coordinates.* 2 edn, (Academic Press, 2001).
54. Vincent, S. R. in *Experimental neuroanatomy* (ed J. P. Bolam) Ch. 7, (Oxford University Press, 1992).
55. Aruga, J., Nozaki, Y., Hatayama, M., Odaka, Y. S. & Yokota, N. Expression of ZIC family genes in meningiomas and other brain tumors. *BMC Cancer* **10**, 79 (2010).
56. Fisher, C. L. & Pei, G. K. Modification of a PCR-based site-directed mutagenesis method. *Biotechniques* **23**, 570–571, 574 (1997).

Acknowledgments

We thank the members of Aruga Laboratory for valuable discussions, Naoko Yamada, Yoshie Ito and Ryoko Takei for technical assistance, and Katsuhiko Mikoshiba for continuous encouragement of our Zic biology project. This work was supported by RIKEN BSI Funds and by a Grant-in-Aid for Scientific Research from the Ministry of Education, Culture, Sports, Science and Technology of Japan. A part of this study is the result of "Development of biomarker candidates for social behavior" carried out under the Strategic Research Program for Brain Sciences by the Ministry of Education, Culture, Sports, Science and Technology of Japan.

Author contributions

M.H. and A.I. characterized the ZIC2 variants. Y.I., T.T. and T.Y. performed the resequencing analysis. A.I., N.T., K.S. Y.S.O., K.Y. and J.A. performed the behavioral analysis. K.S. performed the MRI analysis. Y. N. and J.A. performed the histological analysis. M.H., A.I., K.Y., T.Y. and J.A. wrote the manuscript.

Additional information

Supplementary Information accompanies this paper at http://www.nature.com/scientificreports

Competing financial interests: The authors declare that there are no conflicts of interest associated with the present study.

How to cite this article: Hatayama, M. *et al. Zic2* hypomorphic mutant mice as a schizophrenia model and *ZIC2* mutations identified in schizophrenia patients *Sci. Rep.* 1, 16; DOI:10.1038/srep00016 (2011).

nature neuroscience

Potent amyloidogenicity and pathogenicity of Aβ43

Takashi Saito[1,8], Takahiro Suemoto[1,8], Nathalie Brouwers[2,3], Kristel Sleegers[2,3], Satoru Funamoto[4], Naomi Mihira[1], Yukio Matsuba[1], Kazuyuki Yamada[5], Per Nilsson[1], Jiro Takano[1], Masaki Nishimura[6], Nobuhisa Iwata[1,7], Christine Van Broeckhoven[2,3], Yasuo Ihara[4] & Takaomi C Saido[1]

The amyloid-β peptide Aβ42 is known to be a primary amyloidogenic and pathogenic agent in Alzheimer's disease. However, the role of Aβ43, which is found just as frequently in the brains of affected individuals, remains unresolved. We generated knock-in mice containing a pathogenic presenilin-1 R278I mutation that causes overproduction of Aβ43. Homozygosity was embryonic lethal, indicating that the mutation involves a loss of function. Crossing amyloid precursor protein transgenic mice with heterozygous mutant mice resulted in elevated Aβ43, impairment of short-term memory and acceleration of amyloid-β pathology, which accompanied pronounced accumulation of Aβ43 in plaque cores similar in biochemical composition to those observed in the brains of affected individuals. Consistently, Aβ43 showed a higher propensity to aggregate and was more neurotoxic than Aβ42. Other pathogenic presenilin mutations also caused overproduction of Aβ43 in a manner correlating with Aβ42 and with the age of disease onset. These findings indicate that Aβ43, an overlooked species, is potently amyloidogenic, neurotoxic and abundant *in vivo*.

Alzheimer's disease, the most common form of dementia, is characterized by two pathological features in the brain, extracellular senile plaques and intracellular neurofibrillary tangles. Senile plaques consist of amyloid-β peptide (Aβ) that is generated from amyloid precursor protein (APP) through sequential proteolytic processing by β-secretase and γ-secretase. Two major forms of Aβ exist, Aβ40 and Aβ42, with Aβ42 being more neurotoxic as a result of its higher hydrophobicity, which leads to faster oligomerization and aggregation[1]. A number of mutations associated with early-onset familial Alzheimer's disease (FAD) have been identified in the *APP*, *PSEN1* and *PSEN2* genes, and these mutations lead to accelerated production of Aβ42 or an increase in the Aβ42/Aβ40 ratio. Together, these findings indicate that Aβ42 is essential for the initiation of pathogenesis. However, the possible involvement of longer Aβ species that also exist in the brains of individuals with Alzheimer's disease has not yet been fully investigated.

Thus far, various longer Aβ species, such as Aβ43, Aβ45, Aβ48, Aβ49 and Aβ50, have been qualitatively described in the brains of individuals with Alzheimer's disease[2]. Similar Aβ species have also been found in transgenic mice that overexpress *APP* carrying FAD-linked mutations[3]. Further quantitative studies have revealed that Aβ43 is deposited more frequently than Aβ40 in both sporadic Alzheimer's disease (SAD) and FAD[4–7].

How these Aβ species with different C-terminal ends are generated from the precursor has mainly been investigated by cell biological and biochemical methods. A number of studies[8,9] have found that γ and ε cleavage by γ-secretase controls the fate of the C-terminal end. Aβ43, generated from Aβ49 via Aβ46, is subsequently converted to Aβ40 by γ-secretase, whereas Aβ42 is independently generated from Aβ48 via Aβ45. It has also been reported that the FAD-associated I213T mutation in the *PSEN1* gene increases the generation of longer Aβ species, such as Aβ43, Aβ45 and those even longer than Aβ46, in addition to Aβ42 (ref. 10). It is also noteworthy that Aβ43 appears to be as prone to aggregate *in vitro* as Aβ42 (ref. 11), leading to faster formation of oligomers than occurs in the case of Aβ40 (ref. 12). These observations imply that Aβ43 could be produced as a physiological or pathological metabolite of γ-secretase and may affect Aβ amyloidosis in the brain.

To address whether Aβ43 contributes to Alzheimer's disease pathology, we decided to take advantage of the molecular phenotype of the presenilin-1 (PS1) R278I mutation, as this mutation results in selective overt production of Aβ43 *in vitro*[13], an effect that occurs to a much greater extent than in the case of other mutations, such as R278K, R278S and R278T. The R278I mutation has been independently reported in a pedigree bearing atypical Alzheimer's disease with language impairment[14]. A follow-up survey revealed that one of the affected individuals subsequently progressed to more severe cognitive impairment, and another individual from a different branch of the family with the mutation showed Alzheimer's disease–associated symptoms with an early loss of episodic memory and with a clinical onset of the disease at 59 years of age (M.N. Rossor, University College London, personal communication).

[1]Laboratory for Proteolytic Neuroscience, RIKEN Brain Science Institute, Wako-shi, Saitama, Japan. [2]Neurodegenerative Brain Diseases Group, Department of Molecular Genetics, Flanders Interuniversity Institute for Biotechnology, Antwerpen, Belgium. [3]Laboratory of Neurogenetics, Institute Born-Bunge, University of Antwerp, Antwerpen, Belgium. [4]Faculty of Life Sciences, Doshisha University, Kyoto, Japan. [5]Research Resource Center, RIKEN Brain Science Institute, Wako-shi, Saitama, Japan. [6]Molecular Neuroscience Research Center, Shiga University of Medical Science, Shiga, Japan. [7]Department of Molecular Medicinal Sciences, Division of Biotechnology, Nagasaki University Graduate School of Biomedical Sciences, Nagasaki, Japan. [8]These authors contributed equally to this work. Correspondence should be addressed T.C.S. (saido@brain.riken.jp).

Received 17 March; accepted 13 May; published online 3 July 2011; doi:10.1038/nn.2858

We generated PS1-R278I knock-in mice to assess the biological importance of the mutation and the pathological effect of Aβ43 on Aβ amyloidosis. Homozygosity in knock-in mice was embryonic lethal, presumably because of a partial loss of γ-secretase activity that resulted in a failure in Notch1 processing. Consistent with this, mouse embryonic fibroblasts (MEFs) derived from the homozygous knock-in mice exhibited a failure in PS1 endoproteolysis and Notch1 processing, implying that the particular selectivity of the PS1-R278I mutation for Aβ43 production is closely associated with the partial loss of γ-secretase activity, that is, suppression of the Aβ43-to-Aβ40 conversion, which could also be caused by some of the other PS1 mutations. We crossed heterozygous knock-in mice with APP transgenic mice (APP23 mice carrying the human *APP* isoform 751 transgene harboring the Swedish mutation (K651N M652L)) and found that the progeny exhibited short-term memory loss before plaque formation and developed considerably accelerated amyloid pathology, indicating that Aβ43 is potently amyloidogenic and pathogenic *in vivo*.

RESULTS

Generation of PS1-R278I knock-in mice

To generate PS1 knock-in mice, we constructed a targeting vector carrying a point mutation that results in the replacement of arginine 278 to isoleucine in exon 8 of the *PSEN1* allele (**Supplementary Fig. 1a**). Homologous recombination, germline transmission and genotype were confirmed by Southern blotting and PCR (**Supplementary Fig. 1b,c**). The expression levels of the mutant and wild-type PS1 in the embryonic mouse brains were identical (**Supplementary Fig. 1d**). Unexpectedly, homozygous knock-in (R278I/R278I) was embryonic lethal at embryonic day 15–18 (E15–18; **Fig. 1a**). The mutant embryos showed an overall size reduction, a stubby tail, limb ateliosis and hemorrhage in the CNS as compared with wild-type littermate controls (**Fig. 1a**).

This phenotype is similar to that of PS1-deficient mice and Notch1-related mutant mice[15,16], although the adverse phenotype of the PS1-R278I knock-in mice appeared a few days later than that of PS1-deficient mice. In contrast, we observed no developmental deficits in heterozygous knock-in (+/R278I) mice (**Fig. 1a** and **Supplementary Fig. 2**). The lethal phenotype of the R278I mutation appears to be caused by a loss of developmental function that manifests only under the recessive condition. We generated two lines of double-mutant mice: R278I knock-in/PS1 knockout and M146V knock-in/PS1 knockout. The phenotype of former was embryonic lethal and the latter was normal (**Supplementary Fig. 3a–d**). This observation suggests that the R278 mutation is a loss-of-function mutation. To the best of our knowledge, this is the first case of developmental abnormality being caused by a FAD-linked PS1 point mutation.

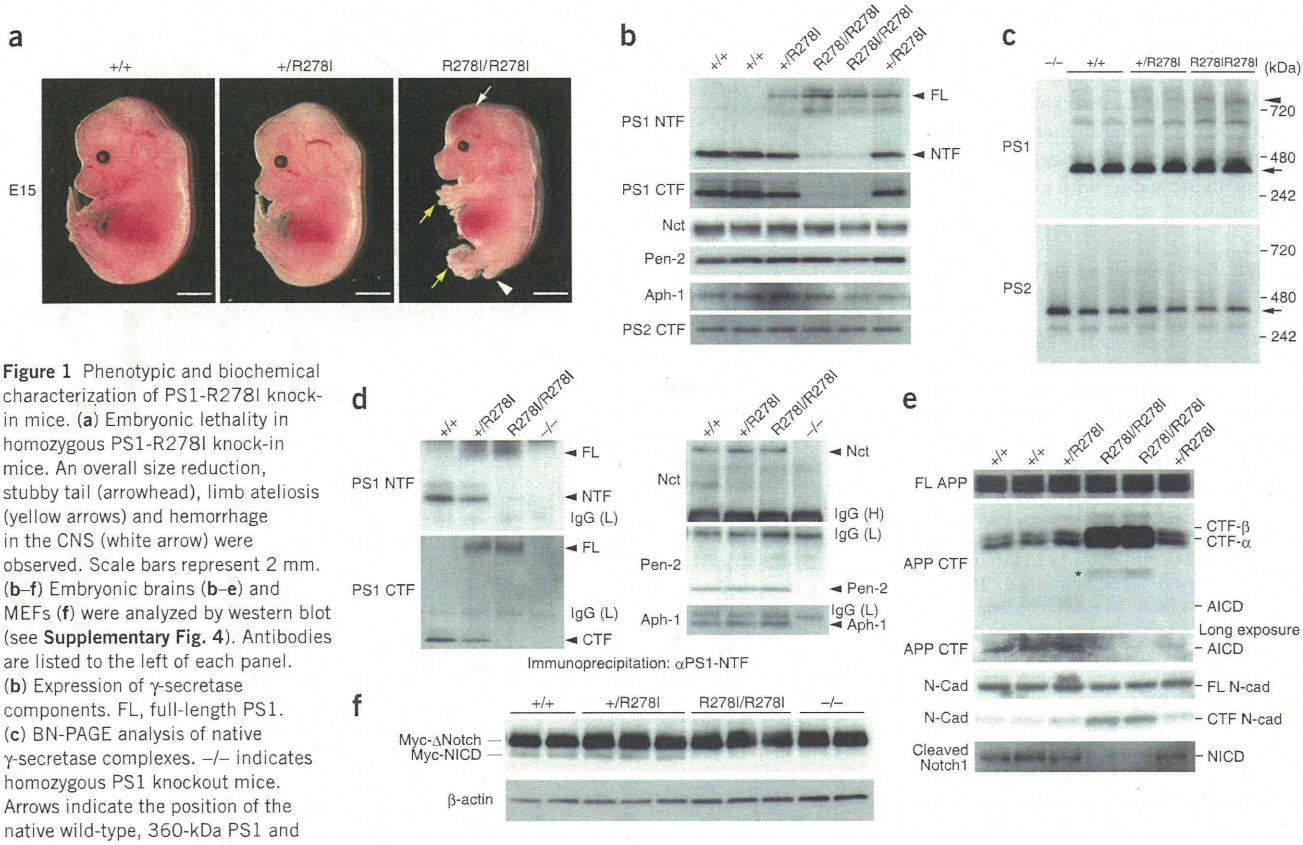

Figure 1 Phenotypic and biochemical characterization of PS1-R278I knock-in mice. (**a**) Embryonic lethality in homozygous PS1-R278I knock-in mice. An overall size reduction, stubby tail (arrowhead), limb ateliosis (yellow arrows) and hemorrhage in the CNS (white arrow) were observed. Scale bars represent 2 mm. (**b–f**) Embryonic brains (**b–e**) and MEFs (**f**) were analyzed by western blot (see **Supplementary Fig. 4**). Antibodies are listed to the left of each panel. (**b**) Expression of γ-secretase components. FL, full-length PS1. (**c**) BN-PAGE analysis of native γ-secretase complexes. –/– indicates homozygous PS1 knockout mice. Arrows indicate the position of the native wild-type, 360-kDa PS1 and PS2 γ-secretase complexes, whereas arrowhead points to the atypical high molecular weight (750 kDa) γ-secretase complex. (**d**) Immunoprecipitation by antibodies to PS1-NTF. IgG(H) and IgG(L) indicate immunoglobulin heavy and light chains, respectively. (**e**) γ-secretase activity in PS1-R278I knock-in brains. Brain extracts were analyzed by western blotting to detect endogenous APP CTF-β, APP CTF-α, APP intracellular domain (AICD), full-length N-cadherin, N-cadherin CTF and NICD products. * indicates an additional signal, smaller than that of CTF-α, which appeared in the knock-in mice. (**f**) Notch1 processing in PS1-R278I knock-in MEFs. Myc-tagged ΔNotch was transiently expressed in the MEFs, and cell lysates were subjected to western blot analysis using antibody to Myc. β-actin levels are shown as internal controls.

Abnormal PS1 endoproteolysis and Notch1 processing

To assess the functional importance of the R278I mutation in the PS1 knock-in line, we analyzed the biochemical properties of PS1-R278I γ-secretase in the embryonic brains before degeneration (**Fig. 1a**). Western blotting revealed a marked decrease in the levels of the N-terminal fragment (NTF) and C-terminal fragment (CTF) of PS1, indicating a failure of PS1 endoproteolysis, in homozygous knock-in brains, whereas the γ-secretase components, including Nicastrin (Nct), presenilin enhancer-2 (Pen-2) and anterior pharynx defective-1 protein (Aph-1), were expressed at normal levels (**Fig. 1b**). The NTF and CTF in the homozygous knock-in mice were, however, clearly detectable, indicating that a fraction of the endoproteolytic activity of PS1 still remained (**Fig. 1b** and **Supplementary Fig. 3e**). It is also noteworthy that the endoproteolysis was partially blocked in the heterozygous PS1-R278I brain, suggesting that the process is at least partly autolytic.

We next investigated whether the PS1-R278I mutation affects the assembly of the γ-secretase complex by Blue Native PAGE (BN-PAGE)[17]. A major signal corresponding to a molecular weight of 360 kDa, the normal molecular weight of the native PS1 γ-secretase complex, was detected in both wild-type and knock-in brains in a manner similar to that of the PS2 γ-secretase complex (**Fig. 1c**). Immunoprecipitation experiments further demonstrated that the mutant PS1 formed a complex with Nct, Pen-2 and Aph-1 (**Fig. 1d**). These data indicate that the PS1-R278I mutation does not affect the formation of the γ-secretase complex. Notably, BN-PAGE detected a minor signal corresponding to a higher molecular weight of 750 kDa in the homozygous knock-in brains (**Fig. 1c**). A similar higher molecular weight signal has been described in preparations from an individual with a deletion of exon 9 in the *PSEN1* gene (PS1-ΔE9)[17] and from SH-SY5Y cells treated with a γ-secretase inhibitor, L-685,458 (ref. 18). PS1-ΔE9 and PS1-ΔT440 also cause PS1 endoproteolytic abnormality in a similar manner to the PS1-R278I mutation[19–21]. The presence of this high molecular weight γ-secretase may reflect a conformational change in the multi-component complex or binding of additional factor(s) to the complex, although its mechanistic involvement remains unclear.

We then examined the effect of the mutation on the metabolism of the γ-secretase substrates. Both the CTF-α and CTF-β of APP and the CTF of N-cadherin accumulated at substantial levels in the homozygous PS1-R278I knock-in mouse brain, but not in the wild-type or heterozygous brains (**Fig. 1e**). Conversely, the APP intracellular domain and Notch1 intracellular domain (NICD) could not be detected in the homozygous knock-in. An additional signal smaller than that of CTF-α appeared in the knock-in mice (**Fig. 1e**), presumably representing an aberrant proteolytic product of CTF-α and CTF-β. These data indicate that the PS1-R278I mutation leads to a substantial loss of γ-secretase activity in a recessive manner.

To further analyze the mutant γ-secretase, we established MEFs from knock-in mice and littermate controls. Western blotting (**Supplementary Fig. 4a**), BN-PAGE (**Supplementary Fig. 4b**) and immunoprecipitation experiments (**Supplementary Fig. 4c**) revealed that the biochemical properties of mutant presenilin in MEFs were

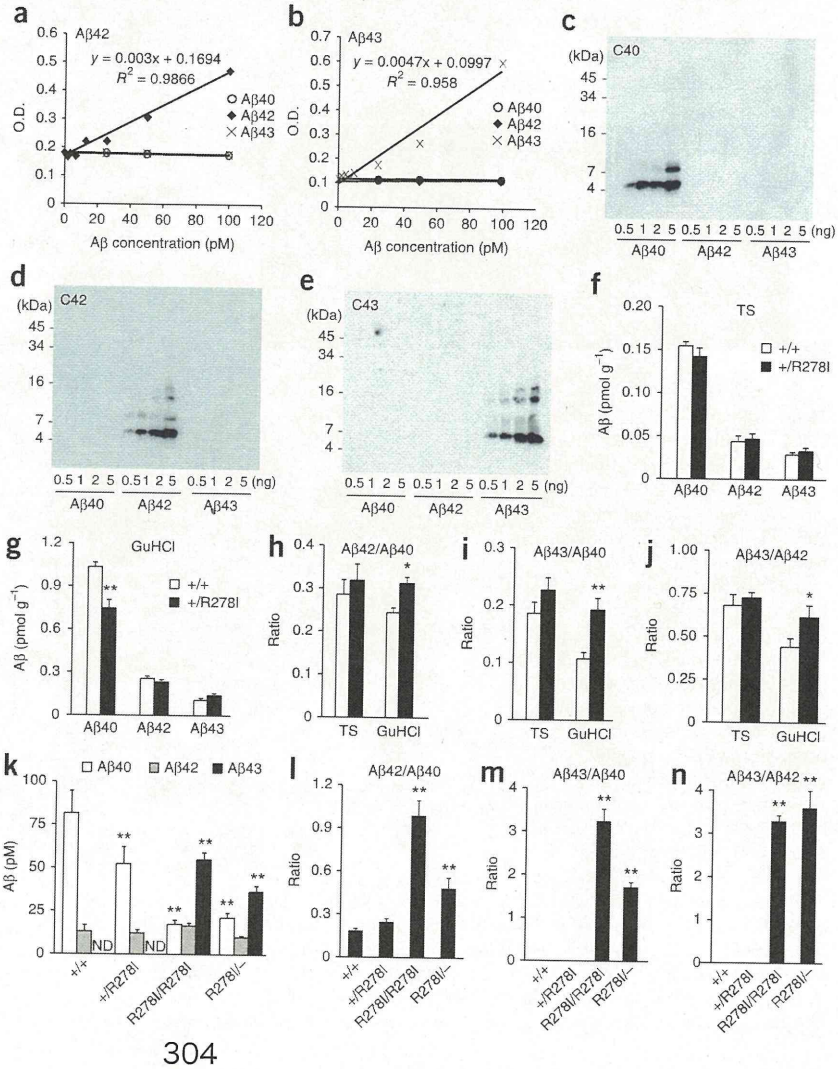

Figure 2 Aβ levels in adult PS1-R278I knock-in mouse brains and MEFs. (**a**,**b**) Establishment of ELISA system to specifically quantify Aβ42 and Aβ43 (see **Supplementary Figs. 6a**,**b** and **7**). (**c**–**e**) Specificity of the antibodies to Aβ40, Aβ42 and Aβ43 used in this ELISA system. Synthetic Aβ1–40, Aβ1–42 and Aβ1–43 were separated by tris/tricine PAGE (15% polyacrylamide gel) and subjected to western blotting. Antibodies to Aβ C40, C42 and C43 specifically recognized Aβ1–40, Aβ1–42 and Aβ1–43, respectively (see **Supplementary Fig. 6c**–**e**). (**f**–**n**) Quantification of Aβ40, Aβ42 and Aβ43 by ELISA in adult mouse brains (**f**–**j**) and MEFs (**k**–**n**). (**f**–**j**) Cortical hemispheres from 24-month-old wild-type and heterozygous knock-in mice were homogenized and fractionated into Tris-HCl–buffered saline–soluble (TS) and GuHCl-soluble fractions. Data represent mean ± s.e.m. ($n = 9$). $^*P < 0.05$ and $^{**}P < 0.01$ between wild-type and heterozygous knock-in mice, Student's t test. (**k**–**n**) Aβ concentrations in conditioned medium from MEFs. We inoculated 8×10^5 cells in a 1-ml culture. The conditioned medium was collected after 24 h and subjected to ELISA. R278I/– indicates a double heterozygote PS1-R278I knock-in × PS1 knockout mice. Data represent mean ± s.d. from two independent experiments ($n = 16$). $^{**}P < 0.01$ compared with wild type, one-way ANOVA with Scheffe's F test. ND, not detected.

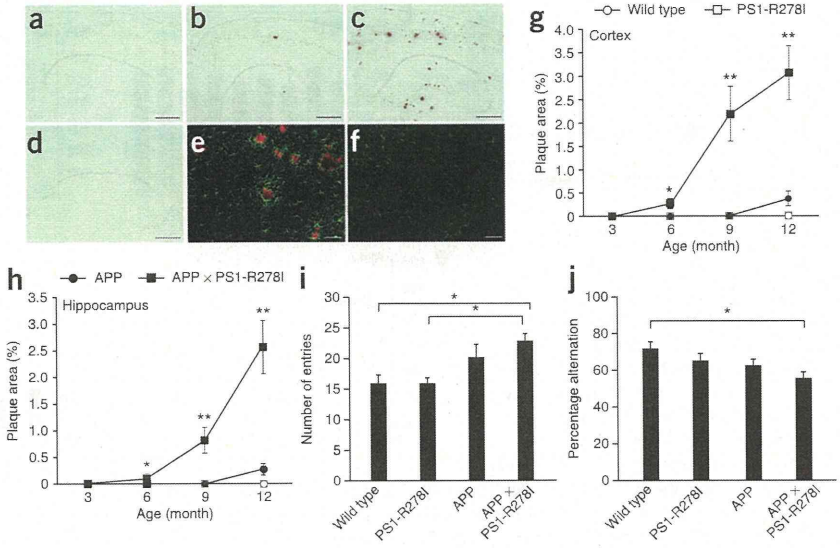

Figure 3 Acceleration of Aβ pathology and short-term memory impairment by the R278I knock-in mutation in APP mice. (**a–f**) Brain sections from APP × PS1-R278I mice (3 (**a**), 6 (**b**) and 9 months (**c**,**d**) old) and 9-month-old single APP mice (**d**,**f**) were immunostained with the 4G8 antibody to Aβ (**a–d**) and antibody to GFAP (green) with 4G8 counterstaining (red) (**e**,**f**). Aβ-immunostained brain sections from cortex (**g**) and hippocampus (**h**) of 3-, 6-, 9- and 12-month-old wild-type, APP and heterozygous PS1-R278I knock-in mice, as well as APP × PS1-R278I mice were analyzed ($n = 5$–6 each genotype). $^{*}P < 0.05$ and $^{**}P < 0.01$ compared with APP mice, two-way ANOVA with Scheffe's F test. Scale bars represent 500 μm (**a–d**) and 50 μm (**e**,**f**). (**i**,**j**) Y-maze test was performed before plaque formation using 3–4-month-old male wild-type, PS1-R278I knock-in, APP and APP × PS1-R278I mice. Data represent mean ± s.e.m. ($n = 10$ each genotype). $^{*}P < 0.05$ compared with wild-type or PS1-R278I knock-in mice, one-way ANOVA with Scheffe's F test.

identical to those in the embryonic brains. We then expressed Myc-tagged ΔNotch1 in the mutant and wild-type MEFs. Western blot analysis revealed that conversion of Myc-ΔNotch1 to Myc-NICD by limited proteolysis occurred in wild-type and heterozygous knock-in MEFs, but not in the homozygous knock-in or PS1 knockout MEFs (**Fig. 1f**). These results indicate that the R287I mutation induces developmental deficits by abolishing of γ-secretase–dependent Notch1 processing.

Aβ40, Aβ42 and Aβ43 in PS1-R278I knock-in brains and MEFs

Because homozygous R278I knock-in mice are embryonic lethal, we went on to analyze adult heterozygous knock-in mice. The adult heterozygous mice were normal in terms of development and anatomy at both 3 and 24 months of age (**Supplementary Fig. 2**), whereas various biochemical properties of PS1, such as partial abnormality of endoproteolysis, the molecular weight of γ-secretase and the identity of the complex components, were identical to those of the heterozygous embryonic brain (**Supplementary Fig. 5**). We then established a specific and highly sensitive ELISA system that could distinguish between Aβ40, Aβ42 and Aβ43 over a broad concentration range (**Fig. 2a,b** and **Supplementary Figs. 6a,b** and **7**). The antibodies that we used were highly specific to each Aβ species (**Fig. 2c–e** and **Supplementary Fig. 6c–e**). Brain tissue fractions that were soluble in Tris-HCl–buffered saline and those that were soluble in 6 M guanidine-HCl (GuHCl) were subjected to quantification.

There was a significant decrease in the steady-state levels of Aβ40 in the GuHCl-soluble fraction in the brains of aged (24 months old) heterozygous PS1-R278I knock-in mice as compared with wild-type animals ($P < 0.01$), although no differences were recorded in the levels of Aβs in the Tris-HCl–buffered saline fraction, or in the levels of Aβ42 and Aβ43 in the GuHCl-soluble fraction (**Fig. 2f,g**). This reduction of Aβ40 in the GuHCl-soluble fraction resulted in a significant elevation of the Aβ42/Aβ40 ($P < 0.05$) and Aβ43/Aβ40 ($P < 0.01$) ratios in the GuHCl-soluble fraction (**Fig. 2h,i**). Notably, the Aβ43/Aβ42 ratio was also significantly increased in the GuHCl-soluble fraction of the heterozygous PS1-R278I knock-in mouse brain ($P < 0.05$; **Fig. 2j**). In younger PS1-R278I knock-in mice (3 months old), Aβ43 levels were too low to detect, although the GuHCl-Aβ40 levels were again significantly reduced in the knock-in mice ($P < 0.05$; **Supplementary Fig. 8**). These results indicate that Aβ43 levels in the mouse brain increase on aging, and that the increase in the Aβ42/Aβ40 and Aβ43/Aβ40 ratios observed in the older heterozygous mice appears to be primarily caused by a decrease in Aβ40. Furthermore, the R278I mutation led to an elevation in the Aβ43/Aβ42 ratio in aged mice. Taken together, these findings indicate that the PS1-R278I mutation gives rise to a modest *in vivo* effect in terms of the levels of endogenous Aβ species under heterozygous conditions.

We next quantified the Aβ variants in conditioned medium from knock-in MEFs (**Fig. 2k–n**). The steady-state levels of Aβ40 were

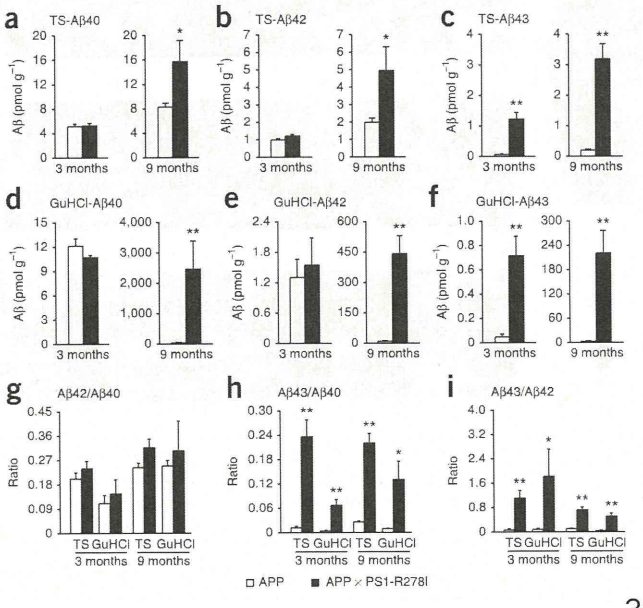

Figure 4 Aβ40, Aβ42 and Aβ43 in APP × PS1-R278I mice. (**a–i**) The levels of Aβ40 (**a**,**d**), Aβ42 (**b**,**e**) and Aβ43 (**c**,**f**) were quantified by ELISA and the ratios of the Aβ species (**g–i**) were subsequently determined. Cortical hemispheres from single APP and APP × PS1-R278I mouse brain (3 and 9 months old) were homogenized and fractionated into Tris-HCl–buffered saline–soluble fractions (**a–c**) and GuHCl-extractable fractions (**d–f**). Data represent mean ± s.e.m. ($n = 7$, 3 months old; $n = 5$, 9 months old). $^{*}P < 0.05$ and $^{**}P < 0.01$ between APP mice and APP × PS1-R278I mice, Student's t test.

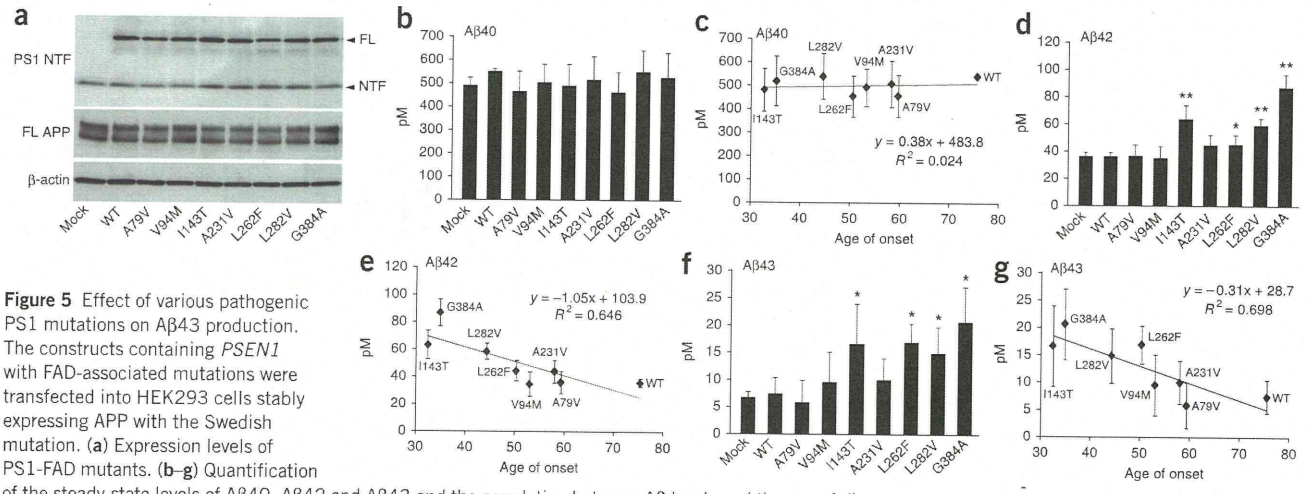

Figure 5 Effect of various pathogenic PS1 mutations on Aβ43 production. The constructs containing *PSEN1* with FAD-associated mutations were transfected into HEK293 cells stably expressing APP with the Swedish mutation. (**a**) Expression levels of PS1-FAD mutants. (**b**–**g**) Quantification of the steady-state levels of Aβ40, Aβ42 and Aβ43 and the correlation between Aβ levels and the age of disease onset. Age of onset is shown as follows: wild type (WT, 75 years old), A79V (59.3), V94M (53), I143T (32.5), A231V (58), L262F (50.3), L282V (44) and G384A (34.9)[24,44]. Data represent mean ± s.d. from five independent series each consisting of duplicate measurements. $*P < 0.05$ and $**P < 0.01$ compared with wild type, one-way ANOVA with Dunnett test.

significantly reduced in a gene dose–dependent manner in the PS1-R278I MEFs as compared with wild-type MEFs ($P < 0.01$). In contrast, Aβ43 markedly increased in the homozygous knock-in MEFs, whereas Aβ42 levels remained unchanged in all genotypes (**Fig. 2k**). Thus, the ratios of longer Aβ species significantly increased in homozygous PS1-R278I knock-in MEFs ($P < 0.01$; **Fig. 2l–n**). Notably, there was no increase in Aβ43 levels in conditioned medium from heterozygous knock-in MEFs (**Fig. 2k**). To unravel the underlying mechanism, we crossed heterozygous R278I knock-in mice with PS1 knockout mice (R278I/–) and measured the levels of Aβs present in conditioned medium from cultured MEFs. Aβ43 levels were increased, implying that wild-type PS1 processes Aβ43 to Aβ40 in heterozygous PS1-R278I knock-in MEFs (**Fig. 2k**). Furthermore, no Aβ43 was detected in heterozygous PS1 knock-out MEFs (data not shown). Together, the data suggests that the γ-secretase substrate can be transferred between separate PS1 molecules or between dimers of PS1, as previously suggested[22], or even between PS1 molecules in the PS1 complexes, for further processing. The fact that total Aβ (Aβ40 + Aβ42 + Aβ43) was decreased in heterozygous knock-in MEFs, as compared with homozygous knock-in MEFs, is of particular interest. This might be a result of a dysfunctional PS1 heterodimer, with wild-type PS1 being either directly affected by PS1-R278I or overloaded with Aβ43 generated by PS1-R278I. Further experiments are required to resolve the reason behind the decreased total Aβ level (**Fig. 2k** and **Supplementary Fig. 9b**). Taken together, our data indicate that the R278I mutation

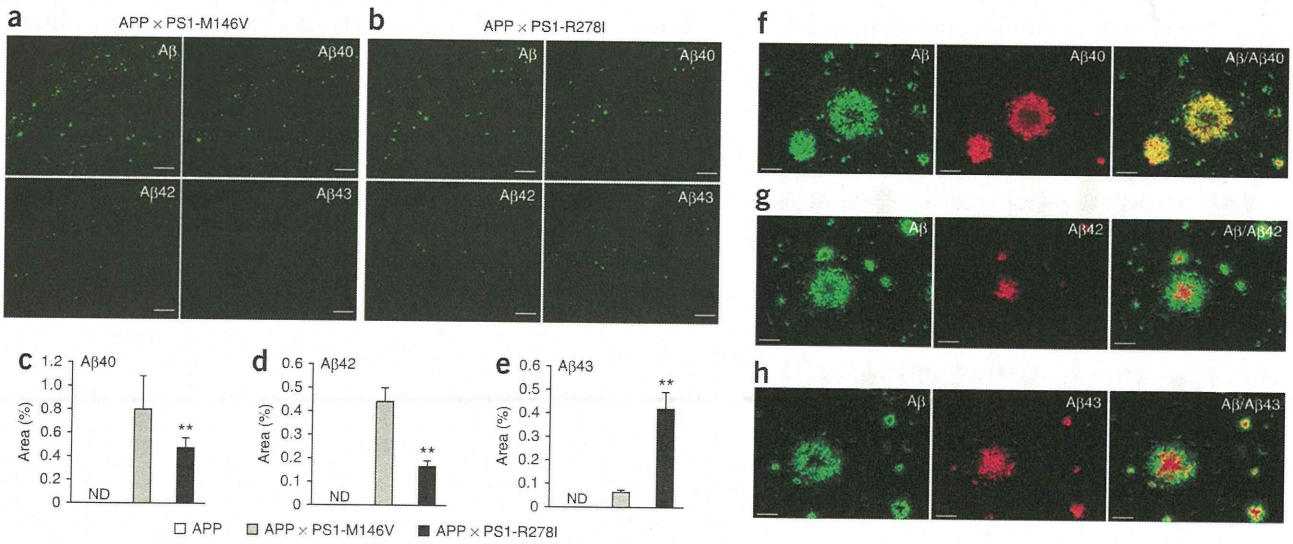

Figure 6 Localization of Aβ species in amyloid plaques of APP × PS1-R278I mice. (**a**,**b**) A set of serial brain sections from 9-month-old APP × PS1-M146V mice (**a**) and APP × PS1-R278I mice (**b**) were immunostained with the following antibodies to Aβ: 4G8 (total Aβ), C40 (Aβ1–40), C42 (Aβ1–42) and C43 (Aβ1–43). (**c**–**e**) The immunoreactive areas in single APP (left), APP × PS1-M146V (middle) and APP × PS1-R278I (right) mice were quantified as indicated ($n = 6$). $**P < 0.01$ between APP × PS1-M146V mice and APP × PS1-R278I mice, one-way ANOVA with Scheffe's F test. ND, not detected. (**f**–**h**) Double-staining with 4G8 (green) and Aβ40 (**f**), Aβ42 (**g**) or Aβ43 (**h**) (red). The images in the left (green) and middle (red) are merged (yellow) on the right. Scale bars represent 500 μm (**a**,**b**) and 50 μm (**f**–**h**).

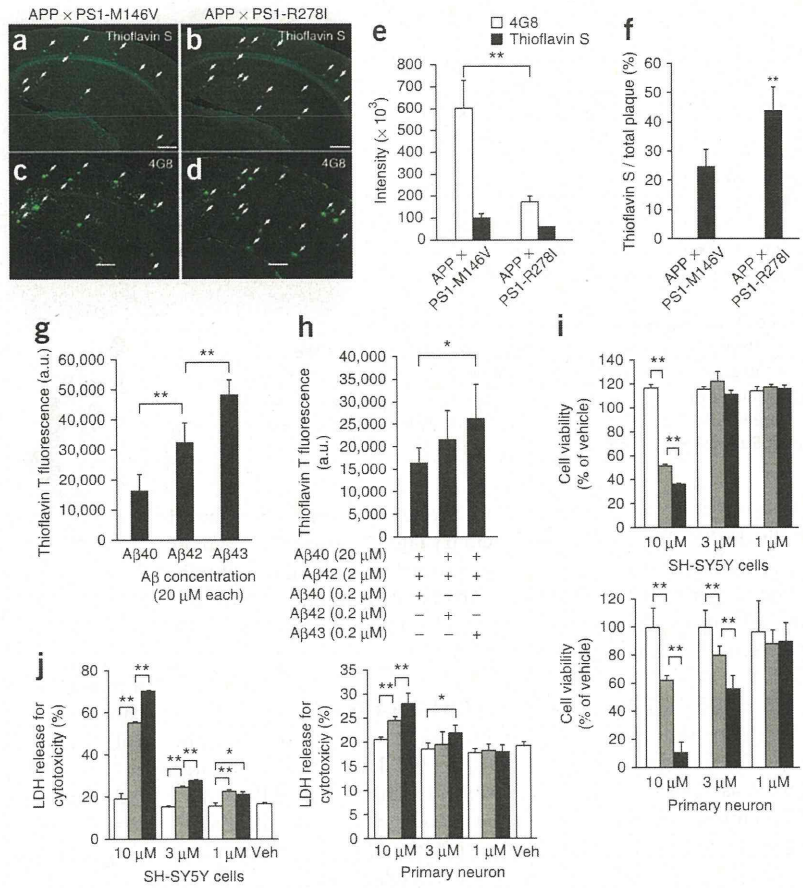

Figure 7 Mature amyloid plaques in APP × PS1-R278I mice and *in vitro* aggregation property and neural cell toxicity of Aβ43. (**a**–**f**) A set of serial brain sections from 9-month-old APP × PS1-M146V mice (**a**,**c**) and APP × PS1-R278I mice (**b**,**d**) were stained with thioflavin S (**a**,**b**) and immunostained with 4G8 (**c**,**d**). Thioflavin S–positive plaque are marked with arrows (**a**,**b**) and the corresponding plaques in the serial brain sections are also marked (**c**,**d**). Scale bars represent 500 μm. (**e**,**f**) The intensity of cortical and hippocampal Aβ immunoreactivity and thioflavin S signals were quantified (**e**), and the ratio of thioflavin S/total Aβ signal of amyloid plaques was determined (**f**) ($n = 12$). Data represent mean ± s.e.m. $^{**}P < 0.01$ between APP × PS1-M146V mice and APP × PS1-R278I mice, Student's *t* test. (**g**,**h**) *In vitro* Aβ aggregation experiments. Incorporation of thioflavin T into Aβ aggregates was measured by fluorescence spectroscopy. The aggregation properties of 20 μM Aβ40, Aβ42 and Aβ43 at 20 μM were measured individually in **g**. The effect of Aβ40, Aβ42 and Aβ43 at a concentration of 0.2 μM on the mixture of 20 μM Aβ40 and 2 μM Aβ42 was then assessed in **h**. Data represent mean ± s.d. from three independent series each consisting of 6–8 individual measurements. $^{**}P < 0.01$ between Aβ40 and Aβ42 or between Aβ42 and Aβ43, $^{*}P < 0.05$ between Aβ40 and Aβ43, one-way ANOVA with Scheffe's *F* test. (**i**,**j**) Neural cell toxicity of Aβ43. Cell viability (**i**) and lactate dehydrogenase (LDH) release as a measure of cell toxicity (**j**) were assayed. Aβs were administrated at 1, 3 and 10 μM, respectively. The results obtained after treatment with Aβ40 (white), Aβ42 (gray) and Aβ43 (black) are indicated, and vehicle (veh) treatment was also indicated by open column in (**j**). Data represent mean ± s.d. from three independent series each consisting of six individual measurements. $^{**}P < 0.01$ between Aβ40 and Aβ42 or between Aβ42 and Aβ43, and $^{*}P < 0.05$ between Aβ40 and Aβ43, two-way ANOVA with Scheffe's *F* test or Dunnett test.

inhibits Aβ43 to Aβ40 conversion, leading to increased Aβ43 levels and concomitant decrease of Aβ40 without altering Aβ42 levels. A similar Aβ-processing pathway has been described previously[9] (**Fig. 2k** and **Supplementary Fig. 10**).

Aβ pathology and memory impairment of APP mice

Overexpression of wild-type human APP in the above-stated MEFs using a semliki-forest virus vector[23] resulted in a significant increase in Aβ43 in the heterozygous R278I knock-in cells ($P < 0.05$; **Supplementary Fig. 9**). The presence of the excessive γ-secretase substrates, that is, APP CTF-α and CTF-β, appeared to force the mutant PS1 to participate in APP processing. These observations prompted us to crossbreed heterozygous PS1-R278I knock-in mice with APP mice to assess the effect of Aβ43 *in vivo*. APP × PS1-R278I mice started to accumulate pathological Aβ deposits at around 6 months of age, whereas it took about 12 months for APP transgenic mice to begin to show signs of such deposition (**Fig. 3a**–**h**). Massive astrocytosis was also detected around the amyloid plaques by 9 months age in the APP × PS1-R278I mice, but not in single transgenic mice (**Fig. 3e**,**f**). Behaviorally, 3–4-month-old APP × PS1-R278I mice exhibited short-term memory impairment as compared with single transgenic mice when their performance was evaluated in a Y-maze test (**Fig. 3i**,**j**). A similar tendency was also observed in the Morris water-maze test, although the difference in this case did not reach statistical significance ($P = 0.051$; data not shown). Taken together, these findings indicate that the PS1-R278I mutation leads to accelerated Aβ pathology with an accompanying inflammatory response and that the cognitive impairment occurs even before plaque formation.

We next quantified the steady-state levels of Aβ40, Aβ42 and Aβ43 in the brains of APP and APP × PS1-R278I mice at 3 and 9 months. Notably, only the double-mutant mice exhibited selective elevation of Aβ43 in both Tris-HCl–buffered saline–soluble and GuHCl-soluble brain fractions at 3 months, which is a time before the pathological deposition of Aβ (**Fig. 4a**–**f**), but by which the double-mutant mice already showed short-term memory impairment (**Fig. 3i**,**j**). In contrast, Aβ40 and Aβ42 levels started to increase at around 9 months. Consequently, both the Aβ43/Aβ40 and Aβ43/Aβ42 ratios were higher in the double mutant mice than in the single APP transgenic mice at both 3 and 9 months, whereas the Aβ42/Aβ40 ratio remained unaltered (**Fig. 4g**–**i**). It is worth noting that the elevation of biochemically detectable Aβ43 levels preceded plaque formation, implying that Aβ43 may be the initial seeding species and the trigger of memory impairment in this mouse model. The steady-state level of Aβ43 also increased in an age-dependent manner in the single APP transgenic mouse brains, beginning before plaque formation (**Fig. 3g**,**h** and **Supplementary Fig. 11**).

In addition, we observed that a variety of FAD-associated PS1 mutations resulted in overproduction of Aβ43 in a manner correlating with

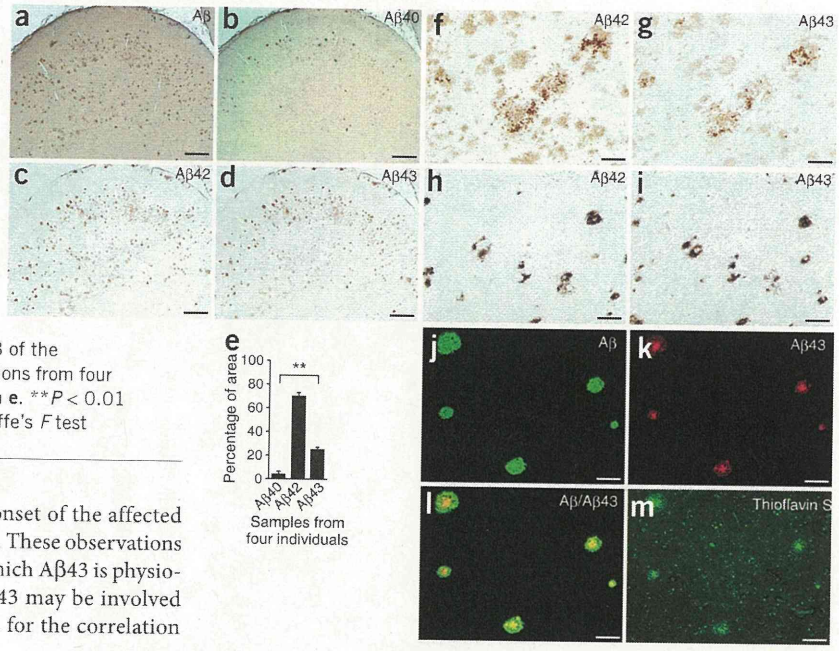

Figure 8 Aβ43 in amyloid plaques in Alzheimer's disease brains. (**a**–**m**) Serial sections of the hippocampal region (**a**–**d**,**h**,**i**,**j**–**m**) and the frontal cortical region of brains from individuals with Alzheimer's disease (**f**,**g**) were stained with 4G8 (total Aβ), C40 (Aβ1–40), C42 (Aβ1–42) and C43 (Aβ1–43), as well as thioflavin S, as indicated. The single staining (**a**–**d**,**f**–**i**) was developed using 3,3′-diaminobenzidine, whereas the double staining (**j**–**m**) used the fluorescent dyes fluorescein (green, Aβ) and rhodamine (red, Aβ43). The images in **j** and **k** are merged (yellow) in **l**. Scale bars represent 250 μm (**a**–**d**) and 25 μm (**f**–**m**). The ratio of Aβ40, Aβ42 and Aβ43 of the plaque areas in the hippocampal region of brain sections from four individuals with Alzheimer's disease were quantified in **e**. $^{**}P < 0.01$ between Aβ40 and Aβ43, one-way ANOVA with Scheffe's *F* test (see **Supplementary Fig. 15**).

the quantity of Aβ42 as well as with the age of onset of the affected individuals[24] (**Fig. 5** and **Supplementary Fig. 12**). These observations suggest that there is an intrinsic mechanism by which Aβ43 is physiologically generated and that both Aβ42 and Aβ43 may be involved in Alzheimer's disease pathogenesis. The reason for the correlation between Aβ42 and Aβ43 remains elusive.

APP × PS1-R278I versus APP × PS1-M146V mice

We generated another line of double-mutant mice by crossbreeding the APP transgenic mice with PS1-M146V knock-in mice, which served as a positive control with which to compare the APP × PS1-R278I mice, as the former mutation results in overproduction of Aβ42 rather than Aβ43 (ref. 25). As expected, the PS1-M146V mutation, unlike the PS1-R278I mutation, resulted in selective accumulation of Aβ42 (**Supplementary Fig. 13**). Although the steady-state levels of Aβ42 in the APP × PS1-M146V mice was about tenfold greater than that of Aβ43 in APP × PS1-R287I mice at 9 months, the total plaque areas, as determined by immunohistochemistry, were similar (**Fig. 6**). Both double-mutant mice accumulated Aβ40 and Aβ42, whereas Aβ43 was much more abundant in the APP × PS1-R278I mice (**Fig. 6a,b**). Quantitative image analyses yielded consistent results (**Fig. 6c–e**). Aβ43 immunoreactivity colocalized with the plaque cores in a manner similar to that of Aβ42, but not to that of Aβ40 (**Fig. 6f–h**). Notably, Aβ species with the third N-terminal residue converted to pyroglutamate (N3pE-Aβ), a potently pathogenic Aβ subspecies[26–29], also colocalized with plaque cores and deposits were more abundant in APP × PS1-R278I than in APP × PS1-M146V mice (**Supplementary Fig. 14**). Although the underlying mechanism that accounts for the elevated N3pE-Aβ generation in the APP × PS1-R278I mice remains unclear, the observation is consistent with a previous finding that some presenilin mutations increase the quantity of N-terminally truncated Aβ in the brains of individuals with FAD[30].

Although APP × PS1-M146V mice accumulated greater numbers of Aβ plaques in the cortical and hippocampal areas than APP × PS1-R278I mice, the density of thioflavin S–positive plaques per total plaques was significantly greater in the APP × PS1-R278I mice ($P < 0.01$; **Fig. 7a–f**). This observation indicates that Aβ43 is even more prone to seed cores in plaque formation than Aβ42. To test this hypothesis *in vitro*, we carried out thioflavin T–binding experiments using an equal amount of Aβ40, Aβ42 and Aβ43 (20 μM each). Aβ43 induced the highest incorporation of thioflavin T into Aβ aggregates (**Fig. 7g**). In addition, stoichiometric experiments, in which we added a relatively small quantity of Aβ40, Aβ42 or Aβ43 (0.2 μM) to a mixture of Aβ40 (20 μM) and Aβ42 (2 μM), revealed that, of the three, Aβ43 most potently accelerated the incorporation of thioflavin T (**Fig. 7h**). These data indicate that Aβ43 contributes to the formation of the thioflavin T–positive β-sheeted structure to a greater extent than either Aβ40 or Aβ42, a finding that may account for the observation that a relatively small amount of Aβ43 is sufficient to accelerate Aβ amyloidosis and induce plaque core formation *in vivo*.

Neural toxicity and amyloid pathology of Aβ43

Consistent with Aβ42 having higher hydrophobicity and higher toxicity than Aβ40 *in vitro* and *in vivo*, a large number of studies have found that Aβ42 contributes to synaptic dysfunctions[31–34]. We therefore compared the toxicity of Aβ40, Aβ42 and Aβ43. Aβ43 showed a higher potent neural toxicity in a dose-dependent manner as compared with Aβ40 and Aβ42 (**Fig. 7i,j**). These results indicate that Aβ43 directly affects neural toxicity and induces synaptic dysfunction, which would contribute to short-term memory impairments before the amyloidogenesis (**Fig. 3i,j**).

Finally, we performed immunohistochemical experiments on brain sections from individuals with SAD to explore the possible involvement of Aβ43 in human neuropathology. Aβ43 accumulated in the brains more frequently than Aβ40 (**Fig. 8a–e** and **Supplementary Fig. 15**), and was present in both diffuse (**Fig. 8f,g**) and dense-cored (**Fig. 8h,i**) plaques, similar to Aβ42 and N3pE-Aβ (**Supplementary Fig. 16a–d**). Furthermore, thioflavin S fluorescence signals colocalized well with Aβ43 immunoreactivity (**Fig. 8j–m**), as well as with N3pE-Aβ (**Supplementary Fig. 16e–g**). These observations are consistent with those of previous studies, which found that a substantial amount of Aβ43 accumulates in SAD and FAD brains[4–7].

DISCUSSION

Previous studies using Bri-Aβ fusion proteins have shown that Aβ42 is essential for amyloid deposition *in vivo*[31] and that Aβ40 inhibits this deposition[32]. The difference between Aβ40 and Aβ42 lies in the C-terminal amino-acid sequence, that is, the additional presence of isoleucine and alanine residues in Aβ42. Because both isoleucine and alanine are hydrophobic amino acids, it is reasonable to assume

that Aβ42 is more prone to form a β-sheet structure than Aβ40. In contrast, the carboxyl-terminal amino acid of Aβ43 is threonine, which carries a hydrophilic alcohol group (together with a hydrophobic methyl group) and could therefore reverse the hydrophobicity of Aβ42. Thus, the amyloidogenicity of Aβ43, a natural product of γ-secretase activity[8,9], has remained elusive.

We focused on Aβ43, an overlooked species in Alzheimer's disease research, and investigated its role in the amyloidogenesis and pathogenesis of Alzheimer's disease. To date, the major focus of research into Alzheimer's disease has been placed on the amyloidogenecity of Aβ42 and, in numerous studies, BC05, an antibody to Aβ42 that has been used to demonstrate that Aβ42 is the major pathogenic species in Alzheimer's disease. As partial crossreactivity of BC05 to Aβ43 had already been reported[35], Aβ42(43) was noted in some of the studies that used BC05. However, many studies have overestimated Aβ42 levels and ignored the possible changes in Aβ43 levels. Almost all FAD-associated PS1 mutations result in an increased Aβ42/Aβ40 ratio that is caused by an increase of Aβ42. However, some of the PS1 mutations lead to a decrease of Aβ40 with or without alteration of Aβ42 levels, which also leads to an increased Aβ42/Aβ40 ratio. One explanation of the association between decreased Aβ40 and FAD could be that Aβ40 is involved in protection from plaque fromation[32]. We found that decreased Aβ40 levels accompanied increased Aβ43 levels in PS1-R278I knock-in mice. Furthermore, the increased Aβ43 levels accelerated Aβ pathology, contributing to the early onset of the disease. Thus, we propose that Aβ43 should be separately analyzed from Aβ42.

In an effort to explore the role of Aβ43 in Aβ amyloidosis, we generated PS1-R278I knock-in mice, as this mutation causes overproduction of Aβ43 *in vitro*[13]. We chose to use this presenilin mutation knock-in procedure rather than the overexpression strategy for the following reasons. First, the R278I mutation is known to be clinically pathogenic. Second, the knock-in procedure is less artificial than transgenic overexpression approaches in general, and the knock-in mice could potentially be used to generate a relevant Alzheimer's disease model by crossbreeding with other mice, such as mutant APP transgenic or knock-in mice. Unexpectedly, the phenotype of the homozygous knock-in mice proved to be embryonic lethal in association with abnormal PS1 endoproteolysis. Limited proteolysis of APP CTF-α and CTF-β, N-cadherin, and Notch1 was also hampered in the homozygous knock-in embryos, although the γ-secretase components appeared to have been properly assembled as a 360-kDa complex. On the basis of previous studies, it appears that the disturbance in Notch1 processing represents the primary cause of the premature death that we observed[16,36]. Compared with PS1 knockout, the embryonic lethality of PS1-R278I knock-in mice occurs at a slightly later stage. Taking into account the fact that a 50% reduction of γ-secretase activity in heterozygous PS1-R278I or in heterozygous PS1 knockout mice does not lead to embryonic lethality and that a 90% reduction in homozygous PS1-R278I mice is lethal, it seems that the γ-secretase activity threshold for survival is somewhere between 10–50% of wild type. The remaining 10% γ-secretase activity in homozygous PS1-R278I knock-in mice could account for the delayed lethality compared with PS1 knockout mice (**Supplementary Fig. 10c**). Taken together, these results strongly suggested that the primary phenotype of the R278I mutation was a partial loss of function of γ-secretase activity.

Despite this, MEFs prepared from homozygous embryos produced extremely high steady-state levels of Aβ43 (approximately 20-fold greater than that of wild-type MEFs); this accompanied a substantial decrease in Aβ40 production and no changes in Aβ42 levels. Previous *in vitro* studies have found that Aβ43 is processed to Aβ40, whereas Aβ42 is independently produced from Aβ45 in the presence of γ-secretase[8,9]. Consistent with these findings, our results from crossbreeding heterozygous PS1-R278I mice with PS1 knockout mice, which showed substantial levels of both Aβ40 and Aβ43, indicate that Aβ43 was indeed converted to Aβ40 independently of Aβ42 production (**Fig. 2k**). Furthermore, we carried out *in vitro* γ-secretase assays and found that the ratio of production of Aβ46 in homozygous PS1-R278I MEFs was increased with a concomitant increase of Aβ43 and decrease of Aβ40 (**Supplementary Fig. 10**), suggesting that production of Aβ40 and Aβ43 also depends on Aβ46 production, as previously postulated[8–10]. Thus, inhibition of this Aβ43-to-Aβ40 conversion could account for the increase in Aβ43 and the concomitant decrease in Aβ40 in the knock-in MEFs. Notably, treatment of PS1-ΔE9–expressing cells with L-685,458 results in elevated Aβ43 production[37], consistent with the notion that multiple processes are involved in the generation of various Aβ species and that a partial loss of γ-secretase activity might give rise to a particular Aβ species. However, *in vitro* γ-secretase activity of heterozygous and homozygous PS1-R278I was markedly reduced in a gene dose–dependent manner, whereas there were no substantial differences in the steady-state levels of total MEF-produced Aβ compared with wild-type MEFs. To elucidate the reason behind this contradiction, it will be necessary to investigate other mechanisms, such as intracellular trafficking and secretion of Aβ, in depth.

The molecular mechanism that allows Aβ43 production, but not other proteolytic processes, remains to be clarified, but it likely involves specific conformational changes of the γ-secretase complex[38]. Because Aβ42 is produced independently of Aβ43 in the presence of γ-secretase, some of the FAD-associated PS1 mutations that cause a decrease in Aβ40 without an increase in Aβ42, such as A79V, A231V, C263F, L282V, L166P and G384A[24,39], might actually result in the elevation of Aβ43 in a manner similar to the R278I mutation. In addition, PS1-ΔE10, an artificial PS1 mutation located to the loop domain of PS1 where R278I is present, leads to a substantial reduction of the steady-state levels of Aβ40 without any alteration of Aβ42 levels, similar to our results; however, Aβ43 levels were not measured[40]. It will therefore be important to investigate whether these FAD-associated mutations give rise to increased Aβ43 levels and to scrutinize their amyloidogenicity. In fact, the I143T, L262F, L282V and G384A mutations did lead to substantial production of Aβ43 in our transfection assays. Notably, Aβ43 levels and the ratio of Aβ43/Aβ40 substantially correlated well with the age of disease onset in a manner similar to Aβ42 levels and the ratio of Aβ42/Aβ40. In addition, a PS1-I143T carrier in a Swedish family with FAD gave rise to high levels of Aβ43 (ref. 7). These observations highlight the possibility that compounds that facilitate the Aβ43-to-Aβ40 and Aβ42-to-Aβ38 conversions might be beneficial for prevention and treatment of Alzheimer's disease by decreasing both Aβ42 and Aβ43. In support of this notion, an oral vaccination with an adeno-associated virus vector carrying Aβ1–43 cDNA was reported to result in a marked reduction of Aβ burdens and improvement of behavioral performances in Tg2576 APP transgenic mice[41,42].

Although we originally thought to generate APP × homozygous PS1-R278I mice, we also explored the possible utility of heterozygous PS1-R278I knock-in mice, given that overexpression of APP in heterozygous PS1-R278I knock-in MEFs resulted in selective elevation of Aβ43. Consistent with this, APP × heterozygous PS1-R278I mice exhibited short-term memory impairment, selective biochemical accumulation of Aβ43 at an early stage before plaque formation and substantial acceleration of Aβ pathology thereafter as compared with APP mice. It should also be noted that the APP × PS1-R278I mice

exhibited a greater density of the thioflavin S–positive signal per plaque than APP × PS1-M146V mice, which overproduced Aβ42 instead of Aβ43. Consistent with previous reports[6,7], we observed Aβ43-positive plaques more often than Aβ40-positive ones in the brains of individuals with Alzheimer's disease. Aβ43 has previously been found in amyloid plaques in individuals with Alzheimer's disease[4,6,7], as well as in aged gorillas[43] and in some Alzheimer's disease model mice harboring PS1 or APP FAD mutations[3,10]. In addition, it has been suggested that the amount of Aβ43 in plaques correlates with cognitive decline[5]. We also found that Aβ43 exhibited potent neural toxicity, comparable to or even greater than that of Aβ42. These findings establish that Aβ43 is indeed amyloidogenic *in vivo* and likely to be pathogenic. Thus, the C-terminal amino acid residue of Aβ43, threonine, appears to strengthen the hydrophobicity of the peptide rather than reversing it.

Notably, biochemical accumulation of Aβ43 preceded pathological deposition in the APP × PS1-R278I mice and in the single APP mice. In addition, the basal Aβ43 levels substantially increased with aging in wild-type mice up to at least 18 months of age (data not shown). These observations suggest that Aβ43 is potentially valuable as a biomarker for presymptomatic diagnosis of Alzheimer's disease. We believe that it would be worth trying to quantify Aβ43 levels in cerebrospinal fluid from individuals with Alzheimer's disease and controls. We also detected the presence of N3pE-Aβ in APP × PS1-R278I mouse brains, a finding that is supported by a previous report quantitatively describing N3pE-Aβ42 and N3pE-Aβ43 in the brains of individuals with FAD or SAD[2]. It is of particular interest that Pittsburgh Compound B, a probe for amyloid imaging by positron emission tomography, selectively binds to N3pE-Aβ[26], implying that N3pE-Aβ42/43 could be particularly prone to seed deposition of other Aβ species, consistent with previous findings[28]. It is also possible that the mutation might affect the interaction of PS1 with other substrates or alter its property of non-γ-secretase activity, such as regulation of neurotransmitter release[29].

In summary, our results indicate that Aβ43, which has largely been overlooked, is potently amyloidogenic and toxic, and highlight the potential value of Aβ43, that is, cerebrospinal fluid Aβ43 levels, as an early marker for some of the detrimental effects of aging in the adult brain. We propose that inhibition of Aβ43 generation, such as by facilitating the conversion of Aβ43 to Aβ40 in the γ-secretase complex, should be beneficial for prevention of Aβ amyloidosis.

METHODS

Methods and any associated references are available in the online version of the paper at http://www.nature.com/natureneuroscience/.

Note: Supplementary information is available on the Nature Neuroscience website.

ACKNOWLEDGMENTS

We thank M.N. Rossor (University College London) for sharing clinical information about the R278I mutation carriers, J.Q. Trojanowski and V.M.-Y. Lee (University of Pennsylvania) for providing postmortem brain tissues, R. Kopan (Washington University) for providing Myc-tagged ΔNotch1 plasmid, A. Takashima (RIKEN Brain Science Institute) for providing antibody to Aph-1, and J. Hardy (University College London) for valuable discussions. This work was supported by research grants from RIKEN Brain Science Institute, the Ministry of Education, Culture, Sports, Science and Technology, the Ministry of Health, Labor and Welfare of Japan, the TAKEDA Science Foundation, the Fund for Scientific Research – Flanders (FWO-V), the Interuniversity Attraction Poles program P6/43 of the Belgian Federal Science Policy Office and a Methusalem Excellence Grant of the Flemish Government to C.V.B. N.B receives a FWO-V postdoctoral fellowship.

AUTHOR CONTRIBUTIONS

This study was jointly designed by T. Saito, T. Suemoto and T.C.S. Experiments were performed by T. Saito, T. Suemoto, N.M., Y.M., K.Y. and S.F. T. Saito, T. Suemoto, S.F., K.Y., P.N., J.T., M.N., N.I., C.V.B., Y.I. and T.C.S. jointly analyzed and interpreted data. N.B., K.S. and C.V.B. identified pathogenic PS1 mutations in patients and families and generated *PSEN1* vector constructs for expression studies.

COMPETING FINANCIAL INTERESTS

The authors declare no competing financial interests.

Published online at http://www.nature.com/natureneuroscience/.
Reprints and permissions information is available online at http://www.nature.com/reprints/index.html.

1. Blennow, K., de Leon, M.J. & Zetterberg, H. Alzheimer's disease. *Lancet* **368**, 387–403 (2006).
2. Miravalle, L. *et al.* Amino-terminally truncated Aβ peptide species are the main component of cotton wool plaques. *Biochemistry* **44**, 10810–10821 (2005).
3. Van Vickle, G.D. *et al.* TgCRND8 amyloid precursor protein transgenic mice exhibit an altered γ-secretase processing and an aggressive, additive amyloid pathology subject to immunotherapeutic modulation. *Biochemistry* **46**, 10317–10327 (2007).
4. Iizuka, T. *et al.* Amyloid β-protein ending at Thr43 is a minor component of some diffuse plaques in the Alzheimer's disease brain, but is not found in cerebrovascular amyloid. *Brain Res.* **702**, 275–278 (1995).
5. Parvathy, S. *et al.* Correlation between Aßx-40-, Aßx-42- and Aßx-43-containing amyloid plaques and cognitive decline. *Arch. Neurol.* **58**, 2025–2032 (2001).
6. Welander, H. *et al.* Aβ43 is more frequent than Aβ40 in amyloid plaque cores from Alzheimer disease brains. *J. Neurochem.* **110**, 697–706 (2009).
7. Keller, L. *et al.* The *PSEN1* I143T mutation in a Swedish family with Alzheimer's disease: clinical report and quantification of Aβ in different brain regions. *Eur. J. Hum. Genet.* **18**, 1202–1208 (2010).
8. Qi-Takahara, Y. *et al.* Longer forms of amyloid β protein: implications for the mechanism of intramembrane cleavage by γ-secretase. *J. Neurosci.* **25**, 436–445 (2005).
9. Takami, M. *et al.* γ-Secretase: successive tripeptide and tetrapeptide release from the transmembrane domain of β-carboxyl terminal fragment. *J. Neurosci.* **29**, 13042–13052 (2009).
10. Shimojo, M. *et al.* Enzymatic characteristics of I213T mutant Presenilin-1/γ-secretase in cell models and knock-in mouse brains: FAD-linked mutation impairs γ-site cleavage of APP-CTFβ. *J. Biol. Chem.* **283**, 16488–16496 (2008).
11. Jarrett, J.T., Berger, E.P. & Lansbury, P.T. Jr. The carboxy terminus of the β amyloid protein is critical for the seeding of amyloid formation: implications for the pathogenesis of Alzheimer's disease. *Biochemistry* **32**, 4693–4697 (1993).
12. Bitan, G. *et al.* Amyloid β-protein (Aβ) assembly: Aβ40 and Aβ42 oligomerize through distinct pathways. *Proc. Natl. Acad. Sci. USA* **100**, 330–335 (2003).
13. Nakaya, Y. *et al.* Random mutagenesis of presenilin-1 identifies novel mutants exclusively generating long amyloid β-peptides. *J. Biol. Chem.* **280**, 19070–19077 (2005).
14. Godbolt, A.K. *et al.* A presenilin 1 R278I mutation presenting with language impairment. *Neurology* **63**, 1702–1704 (2004).
15. Shen, J. *et al.* Skeletal and CNS defects in Presenilin-1-deficient mice. *Cell* **89**, 629–639 (1997).
16. Wong, P.C. *et al.* Presenilin 1 is required for Notch1 and Dll1 expression in the paraxial mesoderm. *Nature* **387**, 288–292 (1997).
17. Culvenor, J.G. *et al.* Characterization of presenilin complexes from mouse and human brain using blue native gel electrophoresis reveals high expression in embryonic brain and minimal change in complex mobility with pathogenic presenilin mutations. *Eur. J. Biochem.* **271**, 375–385 (2003).
18. Evin, G. *et al.* Transition-state analogue γ-secretase inhibitors stabilize a 900 kDa presenilin/nicastrin complex. *Biochemistry* **44**, 4332–4341 (2005).
19. Thinakaran, G. *et al.* Endoproteolysis of presenilin 1 and accumulation of processed derivatives *in vivo*. *Neuron* **17**, 181–190 (1996).
20. Lee, M.K. *et al.* Hyperaccumulation of FAD-linked presenilin 1 variants *in vivo*. *Nat. Med.* **3**, 756–760 (1997).
21. Kaneko, H. *et al.* Enhanced accumulation of phosphorylated α-synuclein and elevated β-amyloid 42/40 ratio caused by expression of the presenilin-1 ΔT440 mutant associated with familial Lewy body disease and variant Alzheimer's disease. *J. Neurosci.* **27**, 13092–13097 (2007).
22. Schroeter, E.H. *et al.* A presenilin dimer at the core of the γ-secretase enzyme: insight from parallel analysis of Notch1 and APP proteolysis. *Proc. Natl. Acad. Sci. USA* **100**, 13075–13080 (2003).
23. Hama, E., Shirotani, K., Iwata, N. & Saido, T.C. Effects of neprilysin chimeric proteins targeted to subcellular compartments on amyloid β peptide clearance in primary neurons. *J. Biol. Chem.* **279**, 30259–30264 (2004).
24. Kumar-Singh, S. *et al.* Mean age-of-onset of familial Alzheimer disease caused by presenilin mutations correlates with both increased Aβ42 and decreased Aβ40. *Hum. Mutat.* **27**, 686–695 (2006).
25. Wang, R., Wang, B., He, W. & Zheng, H. Wild-type presenilin 1 protects against Alzheimer disease mutation–induced amyloid pathology. *J. Biol. Chem.* **281**, 15330–15336 (2006).
26. Maeda, J. *et al.* Longitudinal, quantitative assessment of amyloid, neuroinflammation, and anti-amyloid treatment in a living mouse model of Alzheimer's disease enabled by positron emission tomography. *J. Neurosci.* **27**, 10957–10968 (2007).

27. Saido, T.C. *et al.* Dominant and differential deposition of distinct β-amyloid peptide species, AβN3(pE), in senile plaques. *Neuron* **14**, 457–466 (1995).
28. Schilling, S. *et al.* Glutaminyl cyclase inhibition attenuates pyroglutamate Aβ and Alzheimer's disease–like pathology. *Nat. Med.* **14**, 1106–1111 (2008).
29. Zhang, C. *et al.* Presenilins are essential for regulating neurotransmitter release. *Nature* **460**, 632–636 (2009).
30. Russo, C. *et al.* Presenilin-1 mutations in Alzheimer's disease. *Nature* **405**, 531–532 (2000).
31. McGowan, E. *et al.* Aβ42 is essential for parenchymal and vascular amyloid deposition in mice. *Neuron* **47**, 191–199 (2005).
32. Kim, J. *et al.* Aβ40 inhibits amyloid deposition in vivo. *J. Neurosci.* **27**, 627–633 (2007).
33. Ono, K., Condron, M. & Teplow, D.B. Effects of the English (H6R) and Tottori (D7N) familial Alzheimer disease mutations on amyloid β-protein assembly and toxicity. *J. Biol. Chem.* **285**, 23186–23197 (2010).
34. Jan, A. *et al.* The ratio of monomeric to aggregated forms of Aβ40 and Aβ42 is an important determinant of amyloid-β aggregation, fibrillogenesis, and toxicity. *J. Biol. Chem.* **283**, 28176–28189 (2008).
35. Huppert, S.S. *et al.* Embryonic lethality in mice homozygous for a processing-deficient allele of Notch1. *Nature* **405**, 966–970 (2000).
36. Ikeuchi, T. *et al.* Familial Alzheimer disease-linked presenilin 1 variants enhance production of both Aβ1–40 and Aβ1–42 peptides that are only partially sensitive to a potent aspartyl protease transition state inhibitor of "γ-secretase". *J. Biol. Chem.* **278**, 7010–7018 (2003).
37. Serneels, L. *et al.* γ-Secretase heterogeneity in the Aph1 subunit: relevance for Alzheimer's disease. *Science* **324**, 639–642 (2009).
38. Bentahir, M. *et al.* Presenilin clinical mutations can affect γ-secretase activity by different mechanisms. *J. Neurochem.* **96**, 732–742 (2006).
39. Deng, Y. *et al.* Deletion of presenilin 1 hydrophilic loop sequence leads to impaired γ-secretase activity and exacerbated amyloid pathology. *J. Neurosci.* **26**, 3845–3854 (2006).
40. Hara, H. *et al.* Development of a safe oral Aβ vaccine using recombinant adeno-associated virus vector for Alzheimer's disease. *J. Alzheimers Dis.* **6**, 483–488 (2004).
41. Mouri, A. *et al.* Oral vaccination with a viral vector containing Aβ cDNA attenuates age-related Aβ accumulation and memory deficits without causing inflammation in a mouse Alzheimer model. *FASEB J.* **21**, 2135–2148 (2007).
42. Kimura, N. *et al.* Senile plaques in an aged Western Lowland Gorilla. *Exp. Anim.* **50**, 77–81 (2001).
43. Sturchler-Pierrat, C. *et al.* Two amyloid precursor protein transgenic mouse models with Alzheimer disease–like pathology. *Proc. Natl. Acad. Sci. USA* **94**, 13287–13292 (1997).
44. Huang, S.-M. *et al.* Neprilysin-sensitive synapse-associated amyloid-β peptide oligomers impair neuronal plasticity and cognitive function. *J. Biol. Chem.* **281**, 17941–17951 (2006).

ONLINE METHODS

Generation of PS1-R278I knock-in mice. The genomic DNA of mouse *PSEN1* was isolated from the bacterial artificial chromosome (BAC) library from the 129/Sv mouse genome, and one BAC clone that included introns 5–11 of the *PSEN1* gene was obtained (**Supplementary Fig. 1**). The fragment from the ApaI site of intron 5 to the HindIII site of intron 11 provided the basis for construction of the targeting vector. To introduce the PS1-R278I mutation, we subcloned the SmaI/BamHI fragment containing introns 7 and 8 of the *PSEN1* gene into pBluescript vector. To introduce the R278I mutation, we used 5′-GGT TGA AAC AGC TCA GGA AAT AAA TGA GAC TCT CTT TCC AGC-3′ (underlined, original G to T mutation) as our primer, using GeneEditor Mutagenesis System (Promega) according to the manufacturer's protocol. This fragment was used to replace the original sequence of the *PSEN1* gene. Finally, a *pgk-neo* gene cassette was inserted for positive selection at the EcoRI/SmaI sites located in intron 7, and a diphtheria toxin A fragment cassette was inserted for negative selection at the HindIII site in intron 11. We used the ApaI/EcoRI fragment spanning from intron 5 to intron 7 (4.3 kb) as the long arm and the BamHI/HindIII fragment spanning from intron 8 to intron 11 (3.8 kb) as the short arm of the targeting vector.

Embryonic stem cell cultures and gene-targeting experiments were carried out as described previously. Targeted embryonic stem cells were microinjected into 129/Sv blastocysts. DNA was extracted from the biopsied tail of mouse pups, and the F1 generation of the mutant animals was identified by Southern blot analysis with a 3′ external probe that was produced by PCR using 5′-AAT GGA TAA TCA GAG CCT GCC-3′ and 5′-TCC TCA CAA CTA ACT ACC CAA GG-3′ as primers.

The heterozygous mice were crossbred with EIIa-Cre transgenic mice to remove the *pgk-neo* gene, after which the generated PS1-R278I knock-in mice were backcrossed to the C57BL6/J strain. When the *pgk-neo* gene was removed by Cre excision, a short sequence ranging from the EcoRI to the SmaI sites of intron 7 was also removed. Deletion of this short sequence in intron 7 enables detection of the genotype of mutant mice. To genotype the PS1-R278I knock-in mouse, tail DNA was isolated and subjected to PCR analysis using 5′-AGT TTC AGA CCA GCC TAG GCC AC-3′ and 5′-AGG AAG GGA GAC TTG ACA GC-3′ as primers.

Other mutant mice. PS1 knockout mice and PS1-M146V knock-in mice were purchased from the Jackson Laboratory. APP23 mice carrying the human APP isoform 751 transgene harboring the Swedish mutation (K651N M652L)[45] have been described previously[46]. All animal experiments were carried out according to the RIKEN Brain Science Institute's guidelines for animal experimentation.

MEFs. MEFs were prepared from E13–14 embryos of wild-type, PS1-R278I knock-in and PS1 knockout mice, and inoculated in Dulbecco's modified Eagle medium supplemented with 10% fetal bovine serum (FBS, vol/vol). The conditioned medium and cell lysates from MEFs (passage <8) were subjected to biochemical analyses, including ELISA, native PAGE and western blotting. Transfection of the MEFs with the Myc-tagged ΔNotch construct[47] was performed using FuGENE 6 Transfection Reagent (Roche) according to the manufacturer's instructions.

Blue native-PAGE (BN-PAGE). Non-denaturing native PAGE was performed to confirm the integrity of the γ-secretase complexes[17] using the Novex Bis-Tris gel system (Invitrogen) according to the manufacturer's instructions. Samples were extracted from embryonic brains and MEFs using the sample buffer from the Novex Bis-Tris gel system that contains 1% digitonin. Equal amounts of proteins as determined using the BCA Protein Assay Kit (Pierce) were loaded on a 3–12% gradient Bis-Tris acrylamide gel. Immunoblotting was performed using the antibodies H70 (to the PS1 N terminus, Santa Cruz) and Ab-2 (to PS2, Calbiochem).

Immunoprecipitation assay and western blot analysis. Brain homogenates from embryonic brains (E14–16) and cell lysates of MEFs were immunoprecipitated with H70, and then captured by Dynabead-conjugating protein G (Invitrogen). Immunoprecipitants were subjected to western blot analysis using antibodies H70, MAB5232 (to the PS1 loop, Chemicon), Ab-2, PA1-758 (to Nicastrin, Affinity Bioreagents) and ACS-01 (to Aph1)[10], and antibody to Pen-2 (Zymed). In addition, we used antibody to Aβ1-12 (6E10, Covance), antibody to the N terminus of APP (22C11, Chemicon), antibody to APP CTF (Sigma), antibody to Myc (9B11, Cell Signaling), antibody to Notch1 (mN1A, BD Bioscience) and antibody to β-actin (AC-15, Sigma).

ELISA. Soluble materials from mouse cortical hemispheres were dissolved in Tris-HCl–buffered saline and the insoluble materials were dissolved in guanidine-HCl solution as described previously[48]. Samples from the brains and from the conditioned medium of MEFs were analyzed using an Aβ-ELISA kit (Wako) to quantify Aβ40. To specifically quantify the levels of Aβ42 and Aβ43, we established an Aβ42- and Aβ43-specific sandwich ELISA system using the Aβ-ELISA kit (Wako). Given that BC05, a detection antibody of this kit, cross-reacts with Aβ42 and Aβ43 (ref. 35), we used the Aβ42- and Aβ43-specific antibodies C42 (Aβ42 specific, IBL) and C43 (Aβ43 specific, IBL). The specificities of these antibodies are shown in **Figure 2c–e** and **Supplementary Figure 6c–e**. Samples were incubated overnight at 4 °C in a 96-well plate coated with the capture antibody, BNT77 (antibody to Aβ11–28)[49]. Aβ from samples captured in the ELISA were incubated with C42 or C43 (1:100, 3 h at 20–25 °C), after which horseradish peroxidase–conjugated antibody to rabbit IgG (1:500, 2 h at 20–25 °C) was added as a detection antibody. Synthesized Aβ42 or Aβ43 peptide (Peptide Institute) was used for the preparation of a standard curve, and diluted with the diluents solutions provided in the kit. For consistency, when we quantified the amount of Aβ40, a synthesized Aβ40 peptide (Peptide Institute) was also used for the preparation of a standard curve. This system also worked in broader concentration range of Aβ42 and Aβ43 (**Supplementary Fig. 6a,b**). Furthermore, a highly sensitive Aβ43 system, based on modified protocols, was established for the measurement of samples containing small amounts of Aβ43, such as samples derived from non–APP transgenic mice and cells that are not overexpressing APP (**Supplementary Fig. 7**).

Immunohistochemical and histochemical studies. Paraffin-embedded mouse brain sections were immunostained with 4G8 (antibody to Aβ17-24, Covance), C40 (specific antibody to Aβ40, IBL), C42, C43 and MAB3402 (antibody to GFAP, Chemicon), with or without tyramide signal amplification (PerkinElmer Life Sciences) as described previously[48]. Quantification of immunoreactivity from brain sections were carried out using MetaMorph imaging software (Universal Imaging) as previously described[48].

Y-maze test. Mice were housed individually before transferring to the behavioral laboratory. They were kept during the behavioral analysis. The light condition was 12-h:12-h (lights on 8:00). The laboratory was air-conditioned and maintained at a temperature of approximately 22–23 °C and a humidity of approximately 50–55%. Food and water were freely available except during experimentation. Large tweezers were used to handle mice to avoid individual differences in the handling procedure. All of the experiments were conducted in the light phase (9:00–18:00), and the starting time of the experiments was kept constant.

The Y-maze apparatus (O'Hara) was made of gray plastic and consisted of three compartments (3-cm (width) bottom and 10-cm (width) top, 40 cm (length) and 12 cm (height)) radiating out from the center platform (3 × 3 × 3 cm triangle). The maze was positioned 80 cm above the floor, surrounded by a number of desks and test apparatuses around the maze to act as spatial cues. In this test, each mouse was placed in the center of the maze facing toward one of the arms and was then allowed to explore freely for 5 min. Experiments were performed at a light intensity of 150 lx at the platform. An arm entry was defined as four legs entering one of the arms, and the experimenter counted the sequence of entries by watching a TV monitor behind a partition. An alternation was defined as entry into all three arms on consecutive choices (the maximum number of alternations was the total number of entries minus 2). The percent alternation was calculated as (actual alternations divided by maximum alternations) × 100. The percent alternation was designated as the spontaneous alternation behavior of the mouse, was taken as a measure of memory performance.

Thioflavin T–binding assay. The thioflavin T–binding assay was performed by mixing aliquots of Aβ. Human Aβ1–40, Aβ 1–42 and Aβ1–43 were purchased from the Peptide Institute. We first examined the aggregation properties of Aβ40, Aβ42 and Aβ43 individually by incubating the peptides separately at 20 μM in 50 mM potassium phosphate buffer (pH 7.4) at 37 °C for 24 h with agitation. The stoichiometric effect of different Aβ species on aggregation was investigated in

doi:10.1038/nn.2858

the mixture of Aβ40 and Aβ42 by adding and mixing Aβs in 50 mM potassium phosphate buffer (pH 7.4) at molar concentrations of 20:2:0.2 μM (Aβ40:Aβ42:Aβ40, Aβ42 or Aβ43 = 100:10:1) and incubating them at 37 °C for 24 h with agitation. After incubation, thioflavin T was added to a final concentration of 5 μM and thioflavin T fluorescence was measured at excitation and emission wavelengths of 442 nm and 485 nm, respectively.

Neural cell toxicity assay. Primary cortical neurons were isolated as previously described[23] and plated at a density of 5×10^4 cells per well in 96-well plate ($n = 6$ wells in each experimental conditions). We treated 10–14 d *in vitro* cultures with synthesized Aβ40, Aβ42 and Aβ43 peptide (Peptide Institute) at 0.1 to 10 μM of Aβs for 72 h. These Aβ peptides were dissolved in 10 mM phosphate buffer (pH 7.4, 90%) and 60 mM NaOH (10%), which was used as the vehicle[33]. SH-SY5Y cells were plated at a density of 2×10^4 cells per well with 10% FBS supplemented medium in 96-well plate ($n = 6$ wells in each experimental conditions), and incubated for 24 h. Then the medium was replaced with medium containing 1% FBS (vol/vol), and treated with each Aβ peptides for 48 h. Cell viability was determined using MTS assay (CellTiter 96 Aqueous One Solution Cell Proliferation Assay Kit, Promega)[50], and lactate dehydrogenase release as cell toxicity was performed using CytoTox-ONE Homogeneous Membrane Integrity Assay Kit (Promega)[33], according to the manufacturer's instructions and compared to vehicle treated cells.

Alzheimer's disease brain sections. Post-mortem Alzheimer's disease brain tissues were kindly provided by J.Q. Trojanowski and V.M.-Y. Lee (University of Pennsylvania). The tissues had been fixed with ethanol or formalin and embedded in paraffin. This study was approved by the Institutional Review Board of the RIKEN Brain Science Institute.

45. Kopan, R., Schroeter, E.H., Weintraub, H. & Nye, J.S. Signal transduction by activated mNotch: importance of proteolytic processing and its regulation by the extracellular domain. *Proc. Natl. Acad. Sci. USA* **93**, 1683–1688 (1996).
46. Iwata, N. *et al.* Presynaptic localization of neprilysin contributes to efficient clearance of amyloid-β peptide in mouse brain. *J. Neurosci.* **24**, 991–998 (2004).
47. Iwatsubo, T. *et al.* Visualization of Aβ42(43) and Aβ40 in senile plaques with end-specific Aβ monoclonals: evidence that an initially deposited species is Aβ42(43). *Neuron* **13**, 45–53 (1994).
48. Enya, M. *et al.* Appearance of sodium dodecylsulfate-stable amyloid β-protein (Aβ) dimer in the cortex during aging. *Am. J. Pathol.* **154**, 271–279 (1999).
49. Ryan, D.A., Narrow, W.C., Federoff, H.J. & Bowers, W.J. An improved method for generating consistent soluble amyloid-beta oligomer preparations for *in vitro* neurotoxicity studies. *J. Neurosci. Res.* **190**, 171–179 (2010).
50. Arango, D. *et al.* Systemic genetic study of Alzheimer disease in Latin America: mutation frequencies of the amyloid β precursor protein and presenilin gene in Colombia. *Am. J. Med. Genet.* **103**, 138–143 (2001).

doi:10.1038/nn.2858

Behavioral/Systems/Cognitive

ERK2 Contributes to the Control of Social Behaviors in Mice

Yasushi Satoh,[1] Shogo Endo,[5] Takahiro Nakata,[2] Yasushi Kobayashi,[2] Kazuyuki Yamada,[6] Toshio Ikeda,[7] Atsuya Takeuchi,[3] Takeshi Hiramoto,[4] Yasuhiro Watanabe,[4] and Tomiei Kazama[1]

Departments of [1]Anesthesiology, [2]Anatomy and Neurobiology, [3]Ophthalmology, and [4]Pharmacology, National Defense Medical College, 359-8513 Tokorozawa, Japan, [5]Aging Regulation Research Team, Tokyo Metropolitan Geriatric Hospital and Institute of Gerontology, 173-0015 Tokyo, Japan, [6]Research Resources Center, RIKEN Brain Science Institute, 351-0198 Wako, Japan, and [7]Laboratory of Experimental Animal Model Research, National Center for Geriatrics and Gerontology, 474-8511 Obu, Japan

Signaling through extracellular signal-regulated kinase (ERK) is important in multiple signal transduction networks in the CNS. However, the specific role of ERK2 in *in vivo* brain functions is not fully understood. Here we show that ERK2 play a critical role in regulating social behaviors as well as cognitive and emotional behaviors in mice. To study the brain function of ERK2, we used a conditional, region-specific, genetic approach to target *Erk2* using the Cre/loxP strategy with a *nestin* promoter-driven *cre* transgenic mouse line to induce recombination in the CNS. The resulting *Erk2* conditional knock-out (CKO) mice, in which *Erk2* was abrogated specifically in the CNS, were viable and fertile with a normal appearance. These mice, however, exhibited marked anomalies in multiple aspects of social behaviors related to facets of autism-spectrum disorders: elevated aggressive behaviors, deficits in maternal nurturing, poor nest-building, and lower levels of social familiarity and social interaction. *Erk2* CKO mice also exhibited decreased anxiety-related behaviors and impaired long-term memory. Pharmacological inhibition of ERK1 phosphorylation in *Erk2* CKO mice did not affect the impairments in social behaviors and learning disabilities, indicating that ERK2, but not ERK1 plays a critical role in these behaviors. Our findings suggest that ERK2 has complex and multiple roles in the CNS, with important implications for human psychiatric disorders characterized by deficits in social behaviors.

Introduction

The extracellular signal-regulated kinase (ERK) cascade links transmembrane receptors to downstream effector mechanisms. In neurons, the ERK cascade is activated by stimuli associated with synaptic activity, and in turn activated ERK phosphorylates numerous proteins involved in a diverse array of cellular processes including long-term potentiation, long-term depression, synaptogenesis, and transcriptional and translational regulation (Kelleher et al., 2004; Thomas and Huganir, 2004). Although numerous studies have investigated the role of ERKs in behavioral plasticity, it is controversial whether the ERK isoforms, ERK1 and ERK2, redundantly share their many brain functions and compensate for each other or whether they play distinctive roles. In the analysis of ERK signaling, most experiments use inhibitors of the upstream kinase, MEK. ERK1 and 2 are solely activated by MEK, and thus, it is difficult to examine the specific contribution of each isoform to physiological functions.

Received May 11, 2011; revised June 14, 2011; accepted June 20, 2011.

Author contributions: Y.S. designed research; Y.S., S.E., T.N., Y.K., and A.T. performed research; Y.S., S.E., K.Y., T.I., T.H., Y.W., and T.K. analyzed data; Y.S. and S.E. wrote the paper.

This study was in part performed with support from the Ministry of Education, Culture, Sports, Science and Technology of Japan, the Naito Foundation, and Japan Foundation for Aging and Health. We thank Masako Suzuki, Yuko Ogura, and Kiyoko Takamiya for their excellent technical help; Yayoi Ichiki for her technical assistance in the electron microscopic study, Dr. Kouichi Fukuda for his assistance in animal administration, and Drs. Yuki Takayanagi, Tadashi Kimura, and Kenichi Furuya for advice on the study of maternal behaviors. The *nestin-cre* transgenic mice were a kind gift from Dr. R. Kageyama (University of Kyoto).

Correspondence should be addressed to Dr. Yasushi Satoh, Department of Anesthesiology, National Defense Medical College, 3-2 Namiki, 359-8513 Tokorozawa, Japan. E-mail: ys@ndmc.ac.jp.

DOI:10.1523/JNEUROSCI.2349-11.2011

 0270-6474/11/3111953-15$15.00/0

Recently, however, accumulating evidence has suggested that the role of each isoform in long-term memory may not be functionally redundant. It was demonstrated that *Erk1* knock-out mice did not show a significant impairment in learning ability (Selcher et al., 2001), although the treatment of rodents with a MEK inhibitor impaired memory formation (Kelleher et al., 2004; Thomas and Huganir, 2004). On the other hand, we reported that *Erk2* knockdown mice, in which *Erk2* expression was partially (20–40%) reduced, showed deficits in long-term memory (Satoh et al., 2007).

Although these results suggest a central contribution of the ERK2 isoform to learning and memory, a specific role of ERK2 for other behavioral profile has not been fully revealed *in vivo*. However, accumulating evidence has suggested that the ERK pathway is also involved in regulating emotional/affective behaviors (Ailing et al., 2008; Engel et al., 2009) potentially as an integrator at the nexus of multiple neuronal signaling cascades. Moreover, the relevance of ERK to human psychiatric disorder has been speculated (Kumar et al., 2008; Engel et al., 2009). Considering the complex and pleiotropic involvement of ERK in neuronal functions, it is important to examine the behavioral profile of *Erk2* conditional knock-out (CKO) mice in detail and dissect the roles of ERK1 and ERK2 to understand the clinical relevance.

Because *Erk2* knock-out is embryonically lethal (Satoh et al., 2007), the conditional loss of *Erk2* in the nervous system is of great interest to gain a better understanding of the specific functions of ERK2 *in vivo*. Here, we used a conditional, region-specific, genetic approach to target *Erk2* using the Cre/loxP

strategy with a *nestin* promoter-driven *cre* transgenic mouse line, in which *cre* activity is confined to the CNS.

We found that *Erk2* CKO mice exhibited marked anomalies in social behaviors as well as decreased anxiety-related behaviors and deficits in long-term memory. These anomalies have great relevance to autism-spectrum disorders (ASDs). Our findings suggest pleiotropic roles for ERK2 in neurological and behavioral functions, and that this protein might be a factor underlying human psychiatric disorders.

Materials and Methods

Mice. All experiments were conducted according to the institutional ethical guidelines for animal experiments and the safety guidelines for gene manipulation experiments of the National Defense Medical College and were approved by the Committee for Animal Research at the National Defense Medical College (Tokorozawa, Saitama, Japan). Mice were maintained on a 12 h light-dark cycle (lights on from 7:00 A.M. to 7:00 P.M.) with room temperature at 21 ± 1°C. Mice had *ad libitum* access to water and food.

Generation of floxed Erk2 *and* Erk2 *CKO mice.* The *Erk2* gene was isolated from a 129X1/SvJ mouse genomic library. To generate the *Erk2*(floxN) allele, we constructed a targeting vector from 16.8 kb of *Erk2* DNA (from the ApaI site in intron 1 to the TaqI site in intron 6) (Fig. 1*A*). For positive selection, a floxed (flanked by loxP sites) *Pgk-neo* cassette was inserted in the opposite direction into the EcoRI site in intron 1. A third *loxP* site, KpnI, and SapI sites were inserted into the BglII site in intron 3 (Fig. 1*A*). Targeted insertion of the plasmid by homologous recombination was performed in 129 derived embryonic stem cells (E14), and derived germline targeted offspring ($Erk2^{+/flox(Neo+)}$ mice) were obtained. While the expression of ERK2 in $Erk2^{flox(Neo+)/flox(Neo+)}$ mice was reduced owing to the presence of the *Pgk-neo* cassette (Satoh et al., 2007), it resumed normal levels after excision of the neo cassette by *in vivo* crossing with transgenic mice expressing *cre* recombinase (EIIA-*cre* mice) to obtain mice carrying the *Erk* (*flox(Neo⁻)*) allele ($Erk2^{+/flox(Neo-)}$ mice) or the *Erk2* (Δ*flox*) allele ($Erk2^{+/\Delta flox}$ mice). The disruption of the *Erk2* gene locus was confirmed by Southern blot analysis of genomic DNA from adult mice (Fig. 1*B*,*C*). In the genotyping PCR, the primers used for detection of the *Erk2*(flox) and *Erk2* wild-type alleles were mE2-F3 (5′-GATCTGATGCTTGCCAAAGCC-3′) and mE2-R4 (5′-TGTAAAGTAGCAGCAGATGC-3′) (Fig. 1*D*). The primers used for detection of the *Erk2*(Δflox) allele were mE2-F3 and mE2-R1 (5′-CAGAGTTTCATTATGGAGTCCTCGC-3′) (Fig. 1*D*).

$Erk2^{+/flox(Neo-)}$ mice were backcrossed with C57BL/6J mice for >10 generations. We crossed these mice with *nestin* promoter-driven *cre* transgenic mice (Vernay et al., 2005), which were maintained on the same background (C57BL/6J).

Electron microscopy. Electron microscopy was performed as previously described (Nakata and Yorifuji, 1999). Briefly, under deep anesthesia by intraperitoneal injection of pentobarbital (50 mg/kg), mice (7-weeks of age) were perfused transcardially with 0.1% heparin-PBS followed by a fixative with 2.5% glutaraldehyde, 2% paraformaldehyde in 0.1 M phosphate buffer, pH 7.4. The brains were immediately removed from the skull and cut into coronal slices (1 mm thick). Under a stereomicroscope, small pieces (1 × 1 mm) of the slices were extracted from the hippocampal CA1 or layer II/III of the temporal association cortex (at the levels 2.0 mm caudal to bregma). Then, semithin (200 nm) sections were prepared and stained with 1% toluidine blue. Ultrathin (60–70 nm) sections were cut using an ultramicrotome (Ultracut-N; Reichert-Jung), contrasted with uranyl acetate and lead citrate, examined using a JEM-1010 electron microscope (Jeol) and photographed. At least 20 photomicrographs were analyzed for each mouse to quantify the postsynaptic density (PSD) length, spine number and the percentage of perforated spines.

DiI staining. Lipophilic dye 1,1′-(dioctadecyl-3,3,3′,3′-tetramethylindocarbocyanine perchlorate (DiI) (Invitrogen) staining was performed as described previously (Satoh et al., 2007).

Immunohistochemistry. Immunohistochemical studies were performed as previously described (Satoh et al., 2011). Briefly, paraffin sections (5 μm thick) were deparaffinized and immersed in unmasking solution (Vector H3300; Vector Laboratories) for antigenic retrieval and heated in an autoclave (121°C) for 5 min. Then, sections were incubated with a nonspecific blocking reagent (Dako) for 1 h to reduce background staining.

For bright-field dye staining (Fig. 1*G*), sections were then incubated with a primary antibody (anti-ERK2; mouse monoclonal, 1:1000; BD Transduction Laboratories) overnight in a humidified chamber at 4°C, followed by application of a biotinylated horse anti-mouse IgG secondary antibody (Vector Laboratories). For signal amplification, sections were incubated with an avidin-biotin-horseradish peroxidase complex (ABC Elite kit; Vector Laboratories) and visualized by a 3,3′-diaminobenzidine tetrachloride (Vector Laboratories) reaction according to the manufacturer's instructions. Finally, the sections were counterstained with hematoxylin. PBS was used for rinses.

For fluorescent staining, the primary antibodies used were anti-ERK2 (Fig. 2; rabbit polyclonal, 1:400; Cell Signaling Technology), anti-glial fibrillary acidic protein (GFAP) (see Fig. 4; mouse monoclonal, 1:50; Sigma), or anti-NeuN (Fig. 3; mouse monoclonal, 1:100; Millipore). After application of primary antibody overnight in a humidified chamber at 4°C, sections were incubated with secondary antibodies. The secondary antibodies used were Alexa-Fluor 488-conjugated goat anti-mouse IgG (1:400; Invitrogen) or Cy3-conjugated goat anti-mouse IgG (1:400; Jackson Immunoresearch) for primary antibodies derived from mouse. For primary antibody derived from rabbit, Cy3-conjugated goat anti-rabbit IgG antibody (1:400; Jackson Immunoresearch) was used. Sections were examined with a wide-field or confocal fluorescence microscopy using Nikon C1 system (Nikon). Samples from at least four mice per genotype were examined in each experiment.

Cell counting. Cell number was assessed using the StereoInvestigator system (MicroBrightField). The boundaries were drawn using StereoInvestigator and stained cells were counted within sampling frames chosen in a systematically random manner within the areas of interest. The number of cortical cells stained for NeuN was counted in the dorsolateral portion of the cerebral cortex, from the retrosplenial cortex medially up to the rhinal fissure ventrolaterally.

Western blot analysis. Preparation of protein extracts was performed as previously described (Satoh et al., 2007). Briefly, the amount of protein in each sample was measured using a BCA assay kit (Pierce). Samples were subjected to SDS-PAGE. The proteins were transferred onto an Immobilon-P membrane (Millipore). The blots were then immunoreacted with primary antibodies. The primary antibodies used were anti-ERK1/2 (rabbit polyclonal, 1:1000; Cell Signaling Technology), anti-phospho-ERK1/2 (rabbit polyclonal, 1:1000; Cell Signaling Technology), or anti-β-actin (mouse monoclonal, 1:2500; Sigma). Then, the primary antibodies were recognized using horseradish peroxidase (HRP)-conjugated secondary antibodies. Detection was performed with chemiluminescent substrates for HRP (Super Signal West Pico; Pierce or ECL plus; GE Healthcare). The signals were analyzed using an LAS3000 digital imaging system (Fujifilm). Samples from at least five mice per genotype were examined in each experiment.

Behavioral tests. Mice used for behavioral tests were age-matched male littermates except for the maternal behavior test and pup exchange test. For the maternal behavior and pup exchange test, age-matched female littermates were used. Since the *Erk2* CKO mother does not care well for their pups, all mice used in the behavioral tests were borne and reared by control mothers, except for those used in the pup exchange test. The apparatuses used in this study were made by O'Hara & Co., Ltd. except where described.

Open field test. The open field test was performed as described previously (Satoh et al., 2007). Briefly, activity was measured as the total distance traveled (meters) in 10 min in the open field chamber (50 cm long × 50 cm wide × 40 cm high). The center square of the open field, comprising 50% of the total area, was defined as the "central area" of the open field. Mice used for the test were 9–11 weeks old.

Elevated plus-maze test. The elevated plus-maze (EPM) test was performed as described previously (Satoh et al., 2007). Briefly, mouse behavior was recorded during a 10 min test period. The percentage of time spent in the open arms was used as an index of anxiety-like behavior.

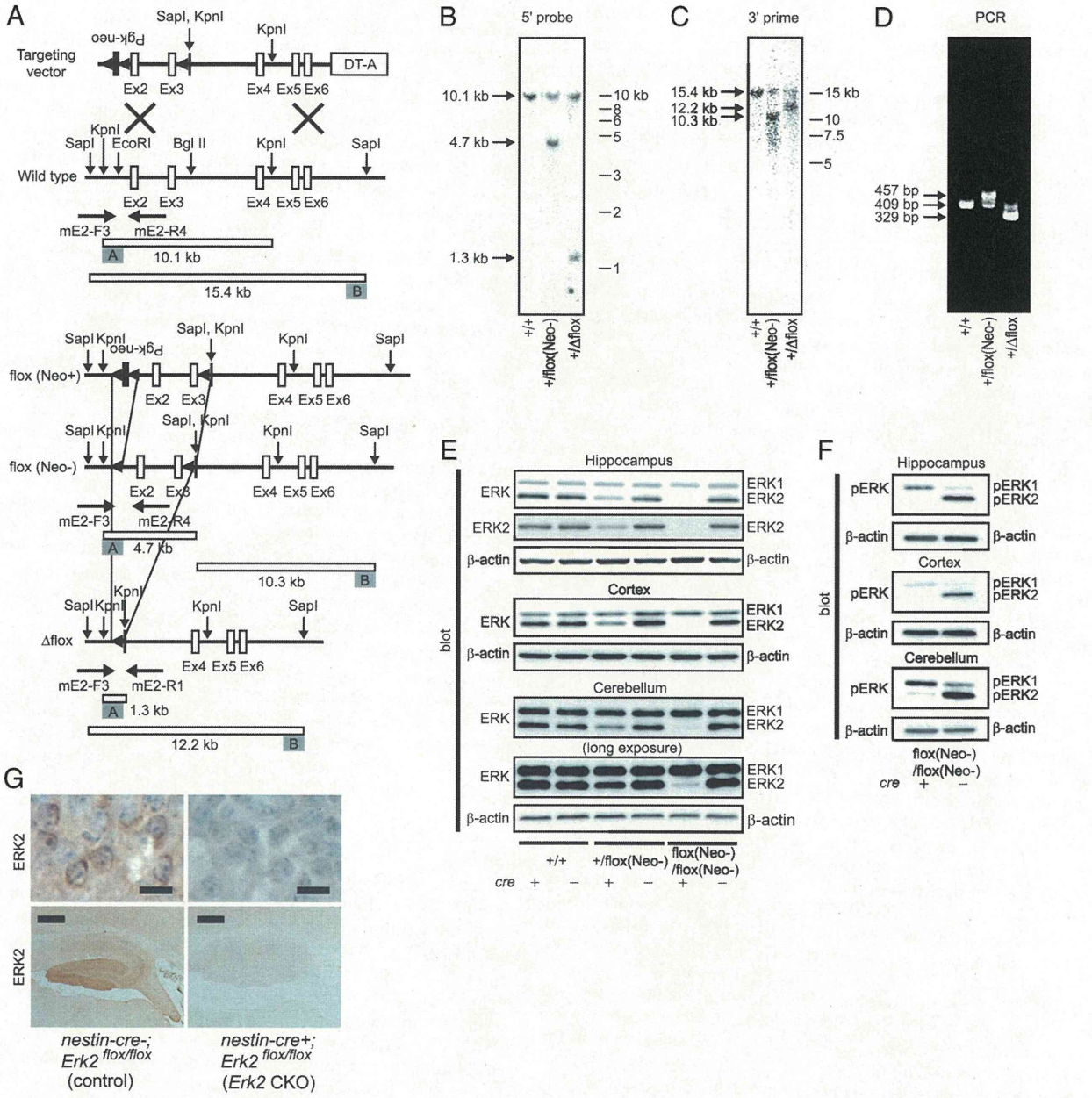

Figure 1. Generation of *Erk2* CKO mice. ***A***, Schematic diagram of targeted knock-out of the mouse *Erk2* gene. The *Erk2*(*flox(Neo+)*) allele is converted to the *Erk2*(*flox(Neo−)*) allele by *in vivo cre*-mediated partial recombination using EIIA-*cre* mice. White boxes represent *Erk2* exons and black boxes represent the *Pgk-neo* cassette. The 5′ and 3′ outer probes used for Southern blotting are shown as gray boxes. The locations of the primers used for genotyping are indicated underneath each scheme. ***B***, ***C***, Southern blot analysis of wild-type and mutant mouse genomic DNA. DNA samples are digested with KpnI and hybridized with the 5′ (***B***) or 3′ (***C***) outer probe. The positions and sizes of the wild-type and mutant fragments are indicated. ***D***, PCR genotyping of wild-type and mutant mice. The positions and sizes of PCR fragments for wild-type and mutant mice are indicated. ***E–G***, Expression profile in adult *Erk2* CKO mice. ***E***, Expression of ERK1 and 2 in extracts of the hippocampus, cortex and cerebellum. ***F***, Phosphorylation status of ERK1 and 2 in basal conditions. In ***E*** and ***F***, β-actin serves as the control for protein loading. ***G***, Loss of ERK2 protein in the nervous system in *Erk2* CKO mice. Immunohistochemical analysis of the hippocampus (bottom) and hippocampal pyramidal cells (top) show the distribution of ERK2 in neuronal cells from *nestin-cre*−; *Erk2* $^{flox/flox}$ (control) mice, and that ERK2 is absent in *nestin-cre*+; *Erk2* $^{flox/flox}$ (*Erk2* CKO) mice. Slides are counterstained with hematoxylin. Scale bars: top, 10 μm; bottom, 500 μm.

Mice used for the test were 9–11 weeks old (the same set of mice as in the open field test).

Maternal behavior test. The maternal behavior test was conducted as described previously (Jin et al., 2007). Briefly, pregnant females were individually housed for a few days before parturition and examined for maternal behavior on the morning of parturition. After a 10 min separation of the mother from her pups, the dam was put in one corner of a cage and three of her pups were placed in different corners of the same cage. Then, she was observed for 20 min with minimal disturbance, and the time spent in crouching over the three pups was recorded. The percentage of newborns scattered was recorded at the end of the test. Mice used for the test were 13–15 weeks old.

Pup exchange test. The pup exchange test was conducted using six *Erk2* CKO and control mother couples. Pups that were born on the same day were exchanged during the first day after birth. The number of surviving pups was followed until weaning. Mice used for the test were 11–15 weeks old.

Resident-intruder test. The resident-intruder test was performed as previously described (Takayanagi et al., 2005). Twenty-week-old resident males were individually housed for 2 weeks before testing. Eight-

week-old wild-type mice, housed in groups, were used as intruders. New intruder mice were used in each test. The attack duration, frequency and latency to first attack were recorded for 10 min.

Social recognition test. The social recognition test was conducted as described previously (Satomoto et al., 2009). We transferred 16-week-old mice from group to individual housing for 7 d before testing to permit establishment of a home-cage territory. Testing began when an ovariectomized female mouse was introduced into the home cage of each male mouse for a 1 min confrontation. At the end of the 1 min trial, the stimulus animal was removed and returned to an individual cage. This sequence was repeated for four trials with 10 min intertrial intervals, and each stimulus mouse was introduced to the same male resident in all four trials. In a fifth trial, another ovariectomized stimulus female was introduced to a resident male mouse. The stimulus females were all wild-type mice. Investigation was defined as direct, active and olfactory exploration of the female by the subject male mice. In general, this consisted of nosing and sniffing of the perioral and anogenital regions, as well as close following and pursuit. Aggressive posturing and sexual behaviors including mounting were not included in the measures of investigation. Females were exposed to only one male per day to reduce male odor contamination.

Sociability test in the open field chamber. The preference for interaction with animate (caged adult mouse) versus inanimate (caged dummy mouse) targets (sociability) was examined in the open field chamber according to a slightly modified method of Kwon et al. (2006). Animate or inanimate targets were put into cylindrical cages allowing olfactory but minimal tactile interaction. The cylindrical cage was 10 cm in height, with a diameter of 9 cm and bars spaced 7 mm apart. Sniffing directed at the cage was scored for 10 min under 70 lux lighting conditions. We used 16-week-old mice in this test and all animate targets were wild-type male mice.

Sociability and social novelty test in a three-room chamber. Social preference for novelty was performed in a three-room chamber as previously described (Moy et al., 2004). Each chamber was 20 cm long × 40.5 cm wide × 30 cm high. Dividing walls were made from clear Plexiglas, with small openings allowing access into each chamber. In the test, mice were initially allowed to explore the chambers for 10 min. After the habituation period, a caged wild-type male mouse, which had no prior contact with the subject mice, was placed in one of the side chambers. The cylindrical cages used were the same as those used in the sociability test in the open field. The subject mouse was placed in the middle chamber, and then the mouse was allowed to interact with an empty cage in one room versus a caged social target in another room for 10 min (sociability test). At the end of the first 10 min session, each mouse was tested in a second 10 min session to quantify social preference for a new stranger (social novelty test). The unfamiliar new stranger mouse was placed in an identical cage in the chamber that had been empty during the first 10 min session. The test mouse had a choice between the first, already-investigated mouse (familiar) and the novel unfamiliar mouse (novel). The time spent in each chamber was measured. Ten-week-old mice were used for the study.

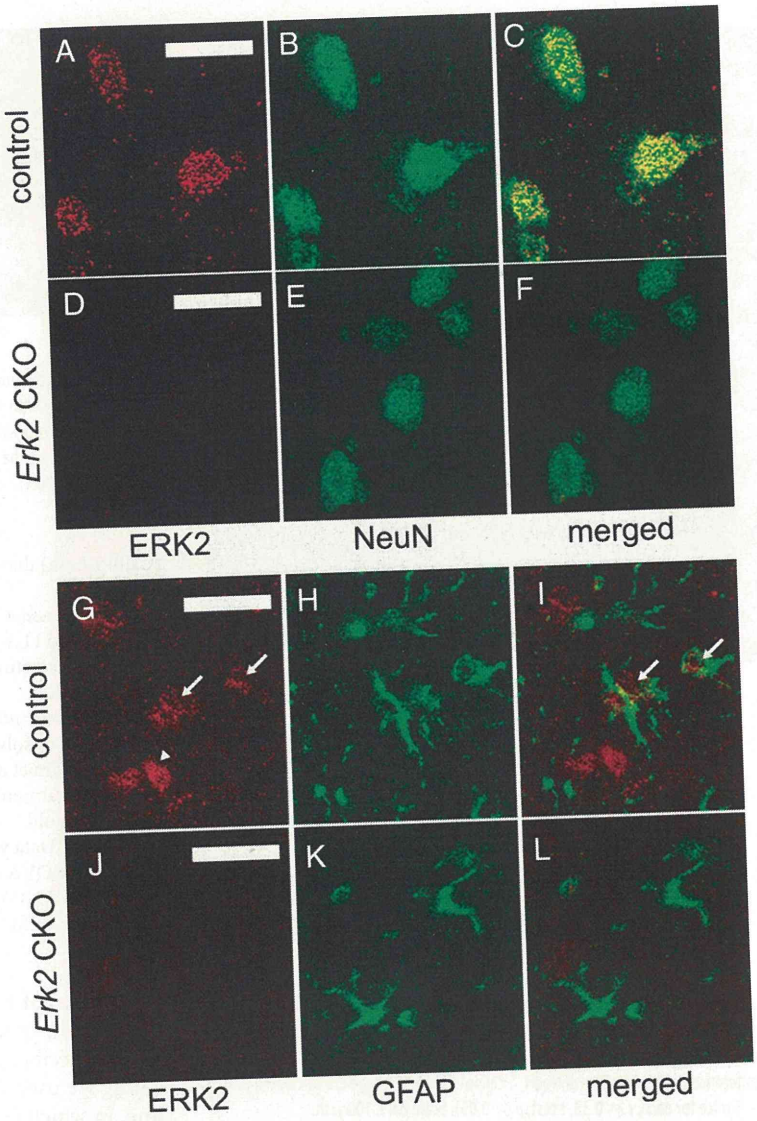

Figure 2. ERK2 protein is abrogated in neuronal and glial cells in *Erk2* CKO mice. ***A–C***, ERK2 is expressed in neuronal cells in control mice at 12 weeks of age. Double staining for ERK2 (***A***) and the postmitotic neuronal marker NeuN (***B***) in the neocortex show that ERK2 is expressed in neurons, as indicated by colocalization (***C***). ***D–F***, ERK2 is abrogated in neuronal cells in *Erk2* CKO mice. Double staining for ERK2 (***D***) and NeuN (***E***) with a merged image (***F***) show that ERK2 is not detectable in neuronal cells in *Erk2* CKO mice. ***G–I***, ERK2 is expressed weakly in astrocytes in control mice. Double staining for ERK2 (***G***) and the astrocyte marker GFAP (***H***) in the neocortex with a merged image (***I***) show partial colocalization of ERK2 and GFAP, indicating that ERK2 is expressed weakly in some astrocytes (arrows) although not in other astrocytes. Arrowhead indicates probable expression of ERK2 in neurons. ***J–L***, ERK2 is abrogated in astrocytes in *Erk2* CKO mice. Double staining for ERK2 (***J***) and GFAP (***K***) with a merged image (***L***) show that ERK2 is not detectable in astrocytes in *Erk2* CKO mice. Scale bars, 20 μm.

Olfactory test. The olfactory test was conducted as described previously (Satomoto et al., 2009). Briefly, mice were habituated to the flavor of a novel food (blueberry cheese) for 3 d before testing. On the fourth day, following 24 h food deprivation, a piece of blueberry cheese was buried under 2 cm of bedding in a clean cage. The mice were placed in the cage, and the time required to find the food was measured. The same set of mice was used as in the sociability and social novelty test in the three-room chamber.

Novelty test. The novelty test was performed as previously described (Satomoto et al., 2009). Mice were housed individually and activity was measured as the total time spent interacting with an inanimate novel object (a small red tube) in 10 min. The same set of mice was used as in the sociability and social novelty test in the three-room chamber.

Nest formation test. Nest formation was examined as described previously (Lijam et al., 1997) with minor modification. Six cages of male controls and six of male *Erk2* CKO mice ($n = 4$ mice per cage) were used

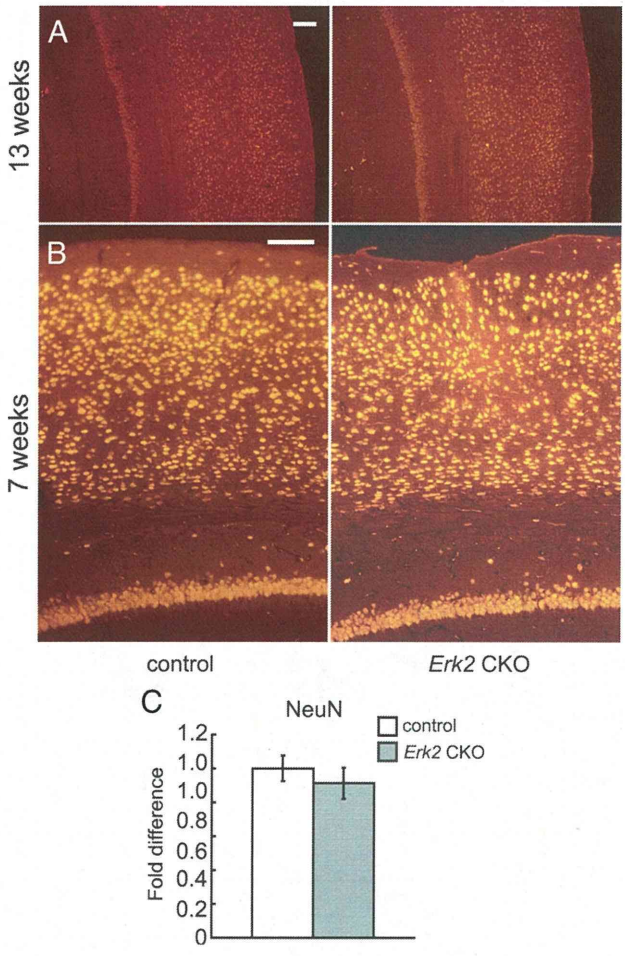

Figure 3. Neuronal number is not altered in *Erk2* CKO mice. ***A***, ***B***, Cortical coronal sections are immunostained for the neuronal marker NeuN. No significant difference is detected in the number of NeuN$^+$ cells between controls and *Erk2* CKO mice at 13 (***A***) and 7 (***B***) weeks of age. ***C***, The fold differences in the numbers of NeuN$^+$ cells at 13 weeks of age are calculated (CKO vs control, $n = 5$ mice for each, $t = 0.33$, t test, $p > 0.05$). Scale bars, 100 μm.

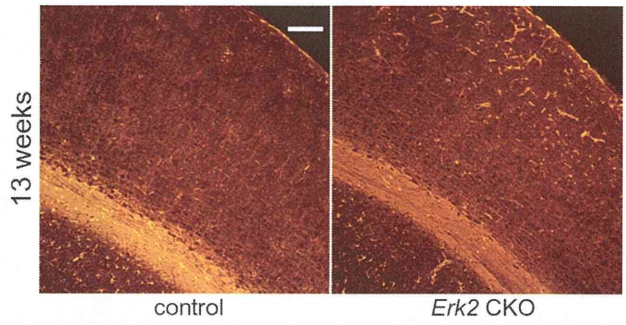

Figure 4. Inactivation of ERK2 results in more astrocytes within the cerebral cortex. Immunohistochemistry with GFAP, a marker for astrocyte, reveals that GFAP immunoreactivity is increased in the cortices of *Erk2* CKO mice compared with controls at 13 weeks of age. Note that GFAP$^+$ cells seem to be more abundant in outer layers than inner layers of cortices in *Erk2* CKO mice. Scale bar, 100 μm.

to evaluate nesting patterns. Small pieces of cotton nesting materials were placed in each cage. After 45 min, nest depth was measured. Mice used for the test were 9–11 weeks old.

Fear conditioning test. The fear conditioning test was performed as previously described (Satoh et al., 2007), with some modifications. Briefly, the conditioning (acquisition) trial for contextual and cued fear conditioning consisted of a 3 min exploration period followed by one or three conditioned stimulus-unconditioned stimulus (CS-US) pairings (US: foot-shock intensity 0.15 mA, duration 1 s; CS: 80 dB white noise, 20 s duration; the US was delivered during the last second of the CS presentation). In the three pairing protocol, each stimulus was separated by 1 min. A context test was performed in the conditioning chamber for 5 min in the absence of white noise at 24 h after conditioning. The level of nonspecific freezing for the context test was monitored for 5 min before the conditioning in the same context. A cued test (for the same set of mice) was performed by presentation of the cue (80 dB white noise, 3 min duration) in an alternative context with distinct visual and tactile cues. The level of nonspecific freezing provoked by the new context was monitored for 3 min before the presentation of the cue in that new context. Mice used for the test were 9–11 weeks old.

MEK inhibitor administration. To examine the effect of blockade of ERK1 activation in *Erk2* CKO mice, MEK was systemically inhibited by intraperitoneal injection of 30 mg/kg SL327 (α-[amino[(4-aminophenyl)thio]methylene]-2-(trifluoromethyl)benzeneacetonitrile) (Calbiochem) dissolved in dimethyl sulfoxide, 1 h before the behavioral tests.

Oxytocin assay. We examined the plasma concentration of oxytocin (Oxt) in 9- to 11-week-old mice. The Oxt assay was performed according to the manufacturer's protocol (Oxytocin Enzyme Immunoassay kit, Assay Designs).

Oxt administration. Mice were treated with acute subcutaneous injection of Oxt dissolved in saline (10 ng per kg body weight) as described previously (Jin et al., 2007). Mouse brain samples were removed 10 min after Oxt treatment for Western blot analyses. Mice used for the test were 9–11 weeks old.

Statistics. Data were analyzed using the Student's t test, Welch's t test, two-way ANOVA with Fisher's *post hoc* test, and two-way repeated measures (RM) ANOVA with Fisher's *post hoc* test. Values are presented as the mean ± SEM.

Results

Generation of *Erk2* CKO mice

To study the function of ERK2 in the CNS, we used a conditional, region-specific, genetic approach to target *Erk2* (Fig. 1*A*). In this study, we used a *nestin* promoter-driven *cre* transgenic mouse line, in which *cre* activity is confined to the CNS (Vernay et al., 2005). The resulting *Erk2* CKO mice (*nestin-cre*+; $Erk2^{flox/flox}$ mice or $Erk2^{\Delta CNS/\Delta CNS}$ mice) were viable and fertile with normal appearance. As anticipated, *Erk2* CKO mice exhibited significantly reduced expression of ERK2 in the cortex, hippocampus and cerebellum compared with littermate controls (Fig. 1*E*,*G*), although a little residual expression of ERK2 was observed in the cerebellum (Fig. 1*E*; cerebellum, long exposure). At the moment, we have no clear explanation for this residual expression, although it is possible that a larger number of *nestin-cre*-unexpressing cells might exist in the cerebellum. The littermate controls used for this study had one of the following genotypes: *nestin-cre*−;$Erk2^{+/+}$, *nestin-cre*−;$Erk2^{flox/flox}$, or *nestin-cre*+; $Erk2^{+/+}$ (hereafter termed control mice). We did not detect any differences among the different genotypes of the control group and we assumed that any phenotypic differences between them would be minimal.

We found no differences in ERK1 expression levels between the brains of *Erk2* CKO and control mice, indicating that there were no compensatory changes in ERK1 expression (Fig. 1*E*). We also evaluated the *in vivo* basal activation state of ERK1 and 2 in brain extracts with an antibody against phospho-ERK1/2 (Fig. 1*F*). In *Erk2* CKO mice, the density of the phospho-ERK1 band was greater than that in the control, suggesting the existence of compensatory upregulation in phosphorylation levels as previ-

ously reported (Lefloch et al., 2008). Although *nestin-cre*−; *Erk2*$^{flox/flox}$ (control) mice were completely normal and showed the expected ERK2 protein expression profile (Fig. 1*G*, upper left and lower left), *Erk2* CKO mice lacked ERK2 immunoreactivity (Fig. 1*G*, upper right and lower right).

We further confirmed that ERK2 protein was abrogated both in neuronal and glial cells in *Erk2* CKO mice by double staining (Fig. 2). ERK2 was expressed in neuronal cells in control mice at 12 weeks of age, as indicated by double staining for ERK2 and NeuN (Fig. 2*A–C*), but ERK2 was abrogated in neurons of *Erk2* CKO mice (Fig. 2*D–F*). Similarly, double staining for ERK2 and the astrocyte marker GFAP in control mice demonstrated slight expression of ERK2 in astrocytes; this expression was absent in *Erk2* CKO mice (Fig. 2*G–L*).

Normal neuronal number with cortical astrogliosis in *Erk2* CKO mice

No significant difference was observed in the neuronal architecture at 7 and 13 weeks of age (Fig. 3*A*,*B*). Then, we examined whether the total number of NeuN-positive (NeuN$^+$) cells in cortices of *Erk2* CKO mice. Numbers of NeuN$^+$ cells were not significantly different between control and *Erk2* CKO mice at 13 weeks of age (Fig. 3*C*; *t* test, $t = 0.51$, $p > 0.05$), indicating that the effect of ERK2 abrogation on the neuronal population was minimal at this age. On the other hand, immunohistochemical analysis using antibody for GFAP revealed that *Erk2* CKO mice contained more GFAP$^+$ cells in their cortices compared with controls at 13 weeks of age (Fig. 4), indicating that ERK2 may be required for regulation of astrogliosis. This is consistent with previous reports, which demonstrated that inhibition of the MEK-ERK pathway resulted in enhanced generation of astrocytes (Paquin et al., 2005; Samuels et al., 2008; Heffron et al., 2009). GFAP$^+$ cells seem to be more abundant in outer layers than inner layers of cortices (Fig. 4), although we do not know the reason.

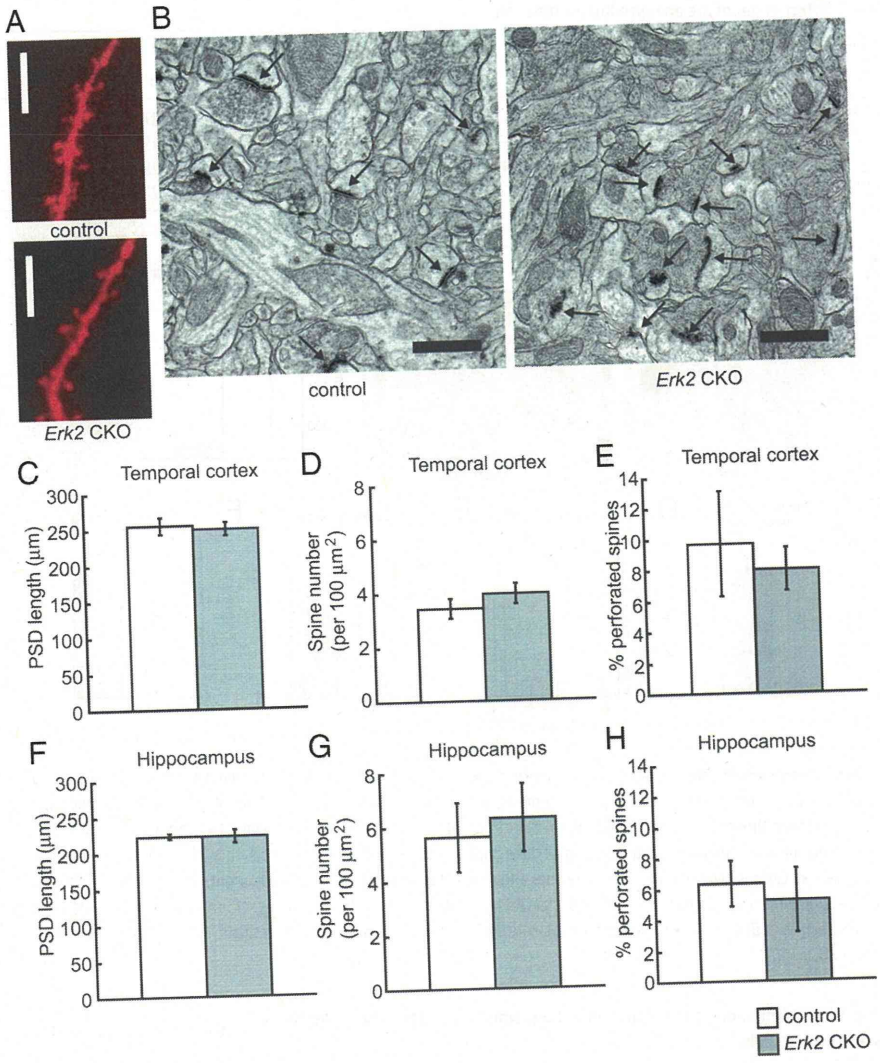

Figure 5. Synaptic density is not altered in *Erk2* CKO mice. ***A***, Representative confocal images of DiI-impregnated dendritic segments of layer II/III neurons from control and *Erk2* CKO mice. No prominent difference is observed in dendritic spines between the genotypes. ***B***, Representative electron micrographs of layer II/III spines in the temporal cortex from control and *Erk2* CKO mice. The postsynaptic density is clearly visible as a dark band located right beneath the postsynaptic membrane in the spine head (arrows). Scale bars: ***A***, 10 μm; ***B***, 1 μm. ***C***, The length of postsynaptic density from layer II/III in the temporal cortex is not significantly different in *Erk2* CKO mice compared with controls. ***D***, The number of spines per 100 μm^2 segments of layer II/III in the temporal cortex is not significantly different between the groups. ***E***, The percentage of perforated spines in apical dendrites of layer II/III in the temporal cortex is not different between the groups. ***F***, The length of postsynaptic density from the hippocampus is not significantly different in *Erk2* CKO mice compared with controls. ***G***, The number of spines per 100 μm^2 segments of the hippocampus is not significantly different between the groups. ***H***, The percentage of perforated spines in apical dendrites of the hippocampus is not different between the groups.

Spine morphology is normal in *Erk2* CKO mice

It has been reported that the ERK pathway might regulate synaptic remodeling (Wu et al., 2001; Goldin and Segal, 2003). Furthermore, the formation and stabilization of dendritic spines via ERK is believed to be involved in long-term storage of information in the CNS (Sweatt, 2004). For instance, the MEK inhibitors PD98059 and U0126 completely prevented a brain-derived neurotrophic factor (BDNF)-induced increase in dendritic spine density (Alonso et al., 2004). Thus we set out to examine the effect of ERK2 abrogation on spine morphology. To examine the number of dendritic spines at the basal level, we used the lipophilic tracer DiI. DiI staining showed that the number of spines per 10 μm dendritic segment in cortical layer II/III was not altered between *Erk2* CKO and control mice (Fig. 5*A*; control, 6.1 ± 0.4, $n = 12$ neurons from four mice; *Erk2* CKO, 6.4 ± 0.5, $n = 12$ neurons from four mice; *t* test, $t = 0.51$, $p > 0.05$). To compare the structure of individual spines between *Erk2* CKO and control mice, we examined spine size using EM. The length of the PSD was used to detect changes in spine size (Meng et al., 2002). In apical dendrites of layer II/III in the temporal cortex, we detected no major changes in the mean PSD length in *Erk2* CKO mice compared with controls (Fig. 5*B*,*C*; control, 255.0 ± 11.5 nm, $n = 5$ mice, total 604 synapses; *Erk2* CKO, 249.9 ± 8.9 nm, $n = 6$

Table 1. Effect of genotype on reproductive function

Pairing		No. of pregnant females observed	No. of pups born	No. of postnatal survivors	Postnatal survivors per total births, %
Male	Female				
Erk2$^{f/f}$; *nestin-cre*+	*Erk2*$^{f/f}$; *nestin-cre*−	67	487	449	92.2
Erk2$^{+/f}$; *nestin-cre*+	*Erk2*$^{+/f}$; *nestin-cre*−	16	115	108	93.9
Erk2$^{+/f}$; *nestin-cre*−	*Erk2*$^{+/f}$; *nestin-cre*+	18	125	80	64.0
Erk2$^{f/f}$; *nestin-cre*−	*Erk2*$^{f/f}$; *nestin-cre*+	24	121	3	2.5

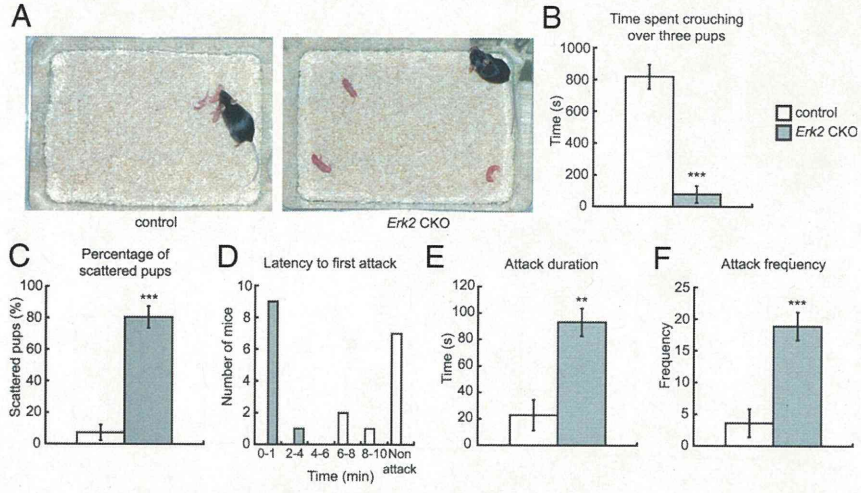

Figure 6. *Erk2* CKO mice are aggressive and impaired in maternal behaviors. ***A–C***, Maternal nurturing in newly postpartum *Erk2* CKO mice. ***A***, In nurturing analysis of postpartum females, a mother is deprived of her first litter of pups for 10 min and then rechallenged with three pups placed individually in the corners of her cage. The typical behavior of a control mother is shown, approaching one pup immediately and collecting all three pups into one corner within a short latency (left), then crouching over them. The *Erk2* CKO mother typically ignores the pups and does not retrieve them immediately (right). ***B***, Time spent crouching over the pups in the nest of control ($n = 10$) and *Erk2* CKO ($n = 10$) mothers. ***C***, The percentage of scattered pups from the same set of mothers as in ***B***. ***D–F***, Aggressive behaviors of male *Erk2* CKO mice as measured by the resident-intruder test (control, $n = 7$; *Erk2* CKO, $n = 7$). $^{**}p < 0.01$, $^{***}p < 0.001$.

Table 2. The number of wounded mice in siblings when reentered into a cage after isolation for 2 weeks

Genotypes of members in the same cage		No. of observed mice	No. of wounded mice	% wounded	No. of mice per cage
Erk2$^{f/f}$; *nestin-cre*−		32	1	3.1	4.0
Erk2$^{f/f}$; *nestin-cre*+	*Erk2*$^{f/f}$; *nestin-cre*−	67	24	35.8	3.9

mice, total 846 synapses; *t* test, $t = 0.39$, $p > 0.05$). In the same area, the number of spines per 100 μm^2 segment was the same in *Erk2* CKO mice and controls (Fig. 5*D*; control, 3.43 ± 0.37, $n = 5$ mice, total 106 areas; *Erk2* CKO, 3.95 ± 0.38, $n = 6$ mice, total 129 areas; *t* test, $t = 1.0$, $p > 0.05$). Larger spines often have a discontinuous PSD and are classified as complex or perforated spines, whereas smaller spines always have a continuous PSD and are classified as simple spines (Calverley and Jones, 1990). In this area, the proportion of perforated spines was not altered in the *Erk2* CKO mice compared with controls (Fig. 5*E*; control, 9.7 ± 3.4%, $n = 5$ mice; *Erk2* CKO, 8.0 ± 1.4%, $n = 6$ mice; *t* test, $t = 0.55$, $p > 0.05$).

Similar to the cortex, we detected no prominent differences in the mean PSD length in pyramidal neurons in stratum radiatum of the hippocampal CA1 area between *Erk2* CKO mice and controls (Fig. 5*F*; control, 222.9 ± 4.0 nm, $n = 5$ mice, total 2432 synapses; *Erk2* CKO, 222.5 ± 9.3 nm, $n = 5$ mice, total 2589 synapses; *t* test, $t = 0.04$, $p > 0.05$). In the same area, the number of spines per 100 μm^2 segment was the same in *Erk2* CKO mice and controls (Fig. 5*G*; control, 5.62 ± 1.28, $n = 5$ mice, total 217 areas; *Erk2* CKO, 6.31 ± 1.26, $n = 5$ mice, total 213 areas, *t* test, $t = 0.39$, $p > 0.05$). In this area, the proportion of perforated spines was not altered in the *Erk2* CKO mice compared with controls (Fig. 5*H*; control, 6.4 ± 1.5%, $n = 5$ mice; *Erk2* CKO, 5.3 ± 2.1%, $n = 5$ mice, *t* test, $t = 0.43$, $p > 0.05$).

These results indicated that spine morphology in the basal state is normal in the temporal cortex and hippocampus of *Erk2* CKO mice.

Maternal nurturing is impaired in *Erk2* CKO mice

We found that whereas *Erk2* CKO mice could bear pups, the majority of pups from *Erk2* CKO dams died neonatally by postnatal day (P) 3, regardless of the genotype of the pups. On the other hand, pups from control mice were viable regardless of the genotype of the pups (Table 1). Because milk was not observed in the digestive tracts of pups from *Erk2* CKO dams, the excess mortality was likely due to defects in lactation. Thus, we investigated the defects in maternal nurturing in *Erk2* CKO mice. In pup exchange test, pups ($n = 40$) born to *Erk2* CKO dams ($n = 6$) were successfully fostered ($n = 39$) when nursed by control dams. On the other hand, pups ($n = 43$) born to control dams ($n = 6$) died when nursed by *Erk2* CKO dams. This indicates that the survival defect in the pups lie entirely with the *Erk2* CKO dams. *Erk2* CKO dams showed a significantly shorter duration of crouching to keep the pups warm and to nurse them (Fig. 6*A*,*B*; *t* test, $t = 5.21$, $p < 0.001$). Significantly more pups from *Erk2* CKO dams were scattered in their home cages (Fig. 6*A*,*C*; *t* test, $t = 8.67$, $p < 0.001$). These results clearly showed abnormal maternal nurturing behavior in postpartum *Erk2* CKO mice.

Erk2 CKO mice display high levels of aggression

When male mice were put together with their siblings after 2 weeks of isolation, some mice were wounded severely. We observed more wounded mice in cages containing *Erk2* CKO mice than those containing only control mice (Table 2), so we assessed the aggressive behavior of *Erk2* CKO mice using the resident-intruder test. *Erk2* CKO resident males attacked the intruder with a shorter latency (Fig. 6*D*), for a longer duration (Fig. 6*E*; *t* test, $t = 3.56$, $p < 0.01$) and with higher frequency (Fig. 6*F*; *t* test, $t = 4.41$, $p < 0.001$) than control residents. These results clearly showed elevated aggressive behavior in *Erk2* CKO mice.

Erk2 CKO mice display abnormal social interactions

We further investigated whether *Erk2* CKO mice display abnormal social interactions. First, we investigated social memory, which, in